BBA - Molecular Basis of Disease 1865 (2019) 661–677

Contents lists available at ScienceDirect

BBA - Molecular Basis of Disease

journal homepage: www.elsevier.com/locate/bbadis

The HCM-causing Y235S cMyBPC mutation accelerates contractile function by altering C1 domain structure

Chang Yoon Doh, Jiayang Li, Ranganath Mamidi, Julian E. Stelzer*

Department of Physiology and Biophysics, School of Medicine, Case Western Reserve University, Cleveland, OH, USA

ARTICLE INFO

Keywords:
Cardiac muscle
Contractile function
Cross-bridge kinetics
Molecular dynamics simulation
In silico modeling

ABSTRACT

Mutations in cardiac myosin binding protein C (cMyBPC) are a major cause of hypertrophic cardiomyopathy (HCM). In particular, a single amino acid substitution of tyrosine to serine at residue 237 in humans (residue 235 in mice) has been linked to HCM with strong disease association. Although cMyBPC truncations, deletions and insertions, and frame shift mutations have been studied, relatively little is known about the functional consequences of missense mutations in cMyBPC. In this study, we characterized the functional and structural effects of the HCM-causing Y235S mutation by performing mechanical experiments and molecular dynamics simulations (MDS). cMyBPC null mouse myocardium was virally transfected with wild-type (WT) or Y235S cMyBPC (KO^{Y235S}). We found that Y235S cMyBPC was properly expressed and incorporated into the cardiac sarcomere, suggesting that the mechanism of disease of the Y235S mutation is not haploinsufficiency or poison peptides. Mechanical experiments in detergent-skinned myocardium isolated from KO^{Y235S} hearts revealed hypercontractile behavior compared to KO^{WT} hearts, evidenced by accelerated cross-bridge kinetics and increased Ca^{2+} sensitivity of force generation. In addition, MDS revealed that the Y235S mutation causes alterations in important intramolecular interactions, surface conformations, and electrostatic potential of the C1 domain of cMyBPC. Our combined in vitro and in silico data suggest that the Y235S mutation directly disrupts internal and surface properties of the C1 domain of cMyBPC, which potentially alters its ligand-binding interactions. These molecular changes may underlie the mechanism for hypercontractile cross-bridge behavior, which ultimately results in the development of cardiac hypertrophy and in vivo cardiac dysfunction.

1. Introduction

Hypertrophic cardiomyopathy (HCM) is a cardiac disease characterized by ventricular hypertrophy, myocyte disarray, and interstitial fibrosis [1]. Recent studies suggest that HCM is estimated to occur > 1 in 200 people worldwide [2,3], and patients with HCM suffer from sudden cardiac death with an annual mortality rate of ~1% [4,5]. Morphologically, HCM causes overall cardiac remodeling and asymmetrical left ventricular thickening [6,7]. Functionally, HCM has been reported to result in varying degrees of phenotypic changes including increased left ventricular ejection fraction [8] as well as associated diastolic dysfunction [9]. The majority of in vitro experiments on myocardia isolated from human HCM patients as well as animal models of HCM have demonstrated increased power output [10], acceleration of cross-bridge (XB) cycling rate [11], and enhanced Ca^{2+} sensitivity of the contractile apparatus, all consistent with hypercontractility [12,13].

The most frequent genetic cause of inherited cardiomyopathies, including HCM, in humans worldwide is the cardiac myosin binding protein C (cMyBPC) gene mutations, accounting for ~50–56% of all cases [14–16]. To date, over 200 mutations have been described with variable penetrance and phenotypes [14]. The majority of cMyBPC-related HCM cases are thought to result in cMyBPC truncation, frame shift, and splice variants causing haploinsufficiency; however, a significant number of mutations (~40%) are single amino acid substitutions [17]. These missense mutations in cMyBPC are often associated with early onset HCM [18]. Although it is known that cMyBPC is a critical modulator of contractile function and disease, its mode of regulation, especially as a result of missense mutations, is incompletely understood.

cMyBPC is made up of eight immunoglobulin-like (Ig-like) and three

Abbreviations: HCM, hypertrophic cardiomyopathy; cMyBPC, cardiac myosin binding protein C; XB, cross-bridge; WT, wild type; PDB, Protein Data Bank; MDS, molecular dynamics simulation

* Corresponding author at: 2109 Adelbert Rd. Robbins E522, Department of Physiology and Biophysics, School of Medicine, Case Western Reserve University, Cleveland, OH 44106, USA.

E-mail address: julian.stelzer@case.edu (J.E. Stelzer).

https://doi.org/10.1016/j.bbadis.2019.01.007
Received 20 August 2018; Received in revised form 18 December 2018; Accepted 2 January 2019
Available online 03 January 2019
0925-4439/

fibronectin-type III (FnIII) domains with cardiac specific inserts [19]. There is evidence that the N-terminal of cMyBPC, encompassing C0, C1, M, and C2 domains, is critical for interacting with S1, proximal S2 or RLC of myosin and with actin in a phosphorylation-dependent manner [20–26], while the C-terminal of cMyBPC is thought to interact with light meromyosin (LMM) and titin [21,27–29]. Recent studies have suggested a critical role for the N-terminal domains of cMyBPC in modulating the magnitude and speed of myocardial force generation [30]. In this regard, the C1 domain in the N-terminal of cMyBPC is thought to be functionally important due to its potential binding interactions with myosin and/or actin [31–33]. The C1 domain has been studied previously through NMR titration and yeast two hybrid (Y2H) experiments. Using ^{15}N-labeled C1 domain combined with shortened S2 (S2Δ), the C-terminal end of the C1 domain was shown to have probable binding region on the positively charged surface of S2Δ [31]. A similar NMR titration analysis using C0C1 fragment and G-actin showed that key residues in the C-terminal end of the C1 domain caused significantly decreased chemical shifts, indicating their interaction [32]. In addition, the Y2H mutational binding assay showed that three lysine residues in C1 domain may be important in actin binding [33]. Furthermore, a recent cryo electron microscope (cryo-EM) structure of domain C0C1 of cMyBPC bound to actin and tropomyosin (TM) suggests that the interaction of a positively-charged four amino acid loop in the N-terminal end of C1 domain with TM may be important in thin filament activation [34]. Overall, many residues that are important for binding myosin and actin appear to be localized in the C-terminal end of the C1 domain, while the N-terminal end seem to play a role in thin filament activation [31–34].

Interestingly, the C1 domain is also known to harbor a large number of pathogenic HCM-causing mutations [35], and most mutations implicated in HCM in the C1 domain are clustered towards the C-terminal end [31]. One such single amino acid mutation located in the C terminal end of the C1 domain is a tyrosine to serine mutation at residue 237 in humans (residue 235 in mouse sequence) first identified in 2003 (mutations are abbreviated with one-letter amino acid code and its residue number, e.g. Y235S) [36]. This missense mutation is caused by an A to C nucleotide transversion in exon 6 of MYBPC3 [14], showing mild familial and strong disease association in humans [36]. The male human proband carrying the Y237S mutation was diagnosed at 37 years old and displayed cardiac hypertrophy, fairly reduced fractional shortening (FS), and left ventricular outflow tract (LVOT) obstruction [36]. A recent study identified an additional mutation of tyrosine 237 to a cysteine (Y237C), where in this case, the human proband was a 33 year old male with a family history of HCM presenting with an aortic murmur and severe hypertrophy [37]. Thus, Y237 mutations in humans cause clinically significant disease phenotypes.

The tyrosine residue 237 is located inside the hydrophobic core of C1 domain, near the C-terminal end, where myosin and/or actin binding occurs. The molecular mechanism of how the Y237S mutation causes disease is unknown; however, based on the disease phenotypes of the Y237S mutation and the position of the tyrosine residue, we can infer that Y237 will have an important role in the development of HCM. Since Y237 participates in a web of hydrogen bonding, hydrophobic and ionic networks, a mutation at the site is expected to destabilize the local structure and possibly cause changes to be propagated across the whole C1 domain [38], thereby affecting the overall cMyBPC function and leading to organ level phenotypic changes described above. Additionally, Y237 is highly conserved across > 25 species in the animal kingdom (Fig. 1) and across all MyBPC isoforms suggesting it is has the potential to be functionally important [39].

Collectively, experimental and clinical studies suggest that single amino acid substitutions in the C1 domain, such as Y237, may impact the structure and overall function of cMyBPC. However, there have been few studies that systematically explored the structure and function of N-terminal cMyBPC missense mutations. Therefore, the goal of this study was to elucidate the functional and structural impact of Y235S in the C1 domain of cMyBPC in the mouse model. Thus, we examined the functional consequences of the HCM-causing Y235S missense mutation in the highly conserved tyrosine residue using a well-established stretch activation protocol. In vitro mechanical experiments were supplemented with molecular dynamics simulations (MDS) and in-depth computational analyses to explore potential molecular mechanisms by which cMyBPC mutations in the C1 domain could cause disease. Ultimately, the combination of multidisciplinary methods aided in providing novel and mechanistic insights into the molecular properties of the Y235S mutation.

2. Materials and methods

2.1. Ethical approval and animal protocols

Experiments were conducted as per the procedures of the Guide for the Care and Use of Laboratory Animals (NIH Publication No. 85–23, Revised 1996), and according to guidelines from the Case Western Reserve University's Institutional Animal Care and Use Committee. Male wild-type (NTG) and cMyBPC null (cMyBPC$^{-/-}$ or KO) SV/129 strain mice, aged 3–7 weeks, were used in this study.

2.2. Preparation and delivery of recombinant lentivirus vectors

The preparation of lentiviruses encoding the full-length mouse cMyBPC or Y235S cMyBPC (cMyBPC^{Y235S}) were generated as previously described [40] using the ViraPower Lentivirus expression system (Invitrogen) according to the manufacturer's instructions. Briefly, a 3.8 kilobase cDNA fragment encoding the complete cDNA copy of murine cMyBPC or Y235S cMyBPC was cloned from a recombinant vector pET 28b (Promega) using PCR TOPO cloning kit (pCR 8/GW/TOPO TA Cloning Kit, K2500-20SC, Invitrogen) in accordance with the manufacturer's instructions. The cMyBPC cDNA and cytomegalovirus (CMV) promoter were cloned into the lentivirus destination vector pLenti6.4/R4R2/V5-DEST using the Gateway approach [40]. Following propagation and purification, the lentivirus was ultra-centrifuged at 25,000 r.p.m. for 2.5 h at 4 °C, using a SW28 rotor. The resulting pellet was resuspended in 60 μl aliquots and stored at −80 °C until use. Virus titer was determined by a Lenti-GOStix kit (Clontech) and SYBR-based qRT-PCR kit (ABM, LV900) according to the manufactures' instructions using an Applied Biosystems RT-PCR platform [40].

To obtain mouse myocardium expressing full-length (KO^{WT}) or Y235S (KO^{Y235S}) cMyBPC, juvenile (3 weeks of age) male cMyBPC$^{-/-}$ mice were anesthetized, intubated, and a thoracotomy was performed to expose the heart to directly inject the myocardium with lentivirus using a syringe with a fine needle tip. A separate set of age-matched cMyBPC$^{-/-}$ mice were injected with a vehicle lentivirus expressing the CMV promotor only, which served as a control. A syringe with a 30 gauge fine needle was inserted into the left ventricular posterior and anterior apex, at a ~50% ventricular tissue depth with the tip of the needle oriented parallel to the apex-base plane of the LV [40]. The tip of the needle was advanced once into the posterior and once into anterior apex, and each time 20 μl of lentivirus was slowly released into the myocardium (2×10^9 CFU/ml) as the syringe was slowly regressed. After virus injection, the syringe was withdrawn, the chest was closed, and negative pleural pressure reestablished before extubation. After four weeks of cMyBPC gene transfer, the mice were euthanized and the hearts were excised. The isolated left-ventricular apices were flash frozen in liquid nitrogen, and stored at −80 °C until later use in protein extraction, immunohistochemistry, and mechanical experiments. All procedures involving animal care and handling were performed according to institutional guidelines set forth by the Animal Care and Use Committee at Case Western Reserve University.

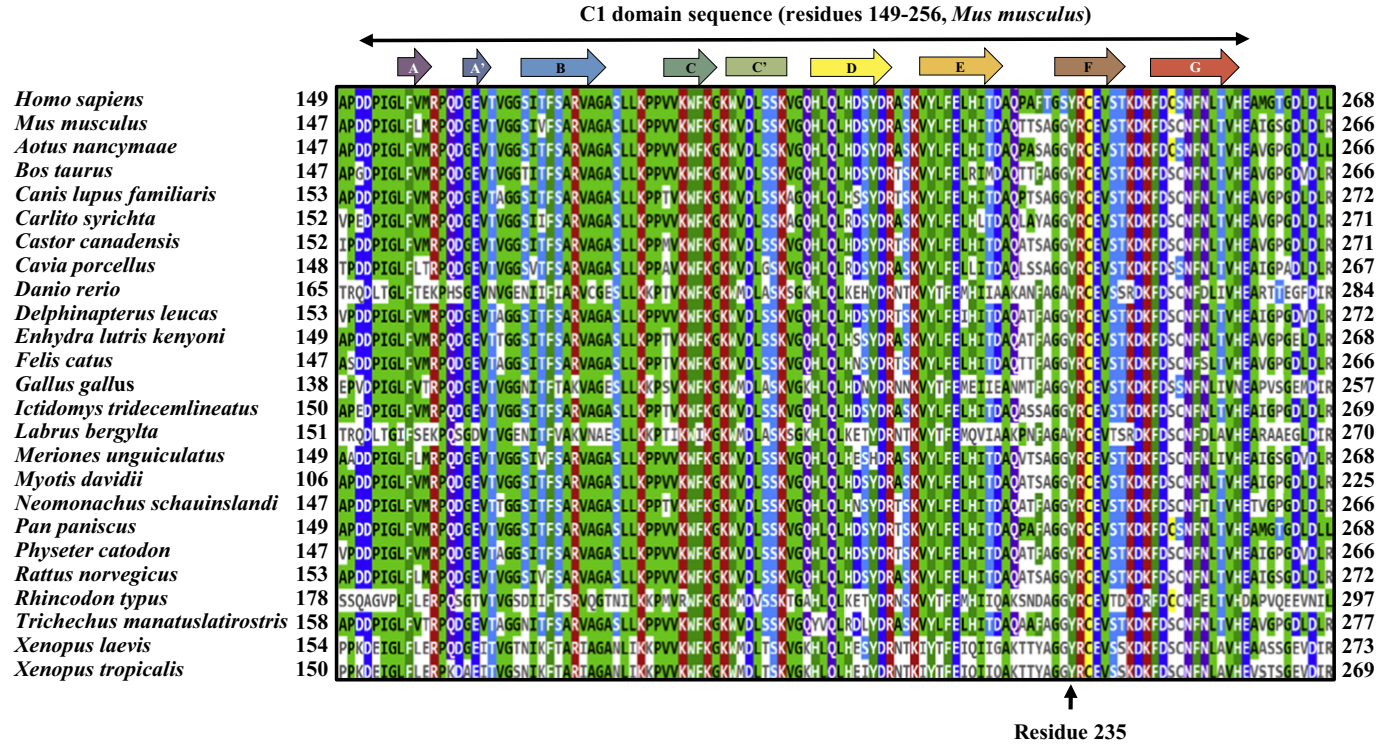

Fig. 1. Multiple sequence alignment of cardiac isoform of myosin binding protein C from 25 species with corresponding NCBI and UniProtKB Accession IDs. *Homo sapiens* (human, AAI51212.1), *Mus musculus* (house mouse, O70468), *Aotus nancymaae* (Nancy Ma's night monkey, XP_021521618.1), *Bos taurus (*cattle, AAI19826.1), *Canis lupus familiaris* (dog, ABB72024.1), *Carlito syrichta* (Philippine tarsier, XP_021564270.1), *Castor canadensis* (North American beaver, XP_020034741.1), *Cavia porcellus* (guinea pig, XP_003465195.2), *Danio rerio* (zebrafish, NP_001037814.2), *Delphinapterus leucas* (beluga whale, XP_022447963.1), *Enhydra lutris kenyoni* (sea otter, XP_022362351.1), *Felis catus* (cat, XP_019667955.1), *Gallus gallus* (red junglefowl, NP_990447.2), *Ictidomys tridecemlineatus* (thirteen-lined ground squirrel, XP_021585283.1), *Labrus bergylta* (Ballan wrasse, XP_020488153.1), *Meriones unguiculatus* (Mongolian gerbil, XP_021496537.1), *Myotis davidii* (vesper bat, ELK23828.1), *Neomonachus schauinslandi* (Hawaiian monk seal, XP_021540477.1), *Pan paniscus* (bonobo, XP_003815230.1), *Physeter catodon* (sperm whale, XP_007113025.1), *Rattus norvegicus* (brown rat, NP_001099960.1), *Rhincodon typus* (whale shark, XP_020385793.1), *Trichechus manatuslatirostris* (West Indian manatee, XP_004387787.1), *Xenopus laevis* (African clawed frog, AAL15871.1), and *Xenopus tropicalis* (Western clawed frog, NP_001106379.1). Region of homology modeling using 3CX2 is shown with a double sided black arrow. Secondary structures are shown on top of the alignment with colored arrows (β sheets) and rectangles (3^{10}-helix). The tyrosine residue 235 (in mouse sequence) is conserved 100% across 25 species.

2.3. Cardiac sample preparation and PKA phosphorylation

Cardiac myofibrils were isolated from frozen mouse hearts on the day of the experiment. Frozen ventricular tissue chunks were homogenized for ~20 s using a homogenizer (PowerGen 500; Thermo Fischer Scientific) in fresh relaxing solution (in mM: 100 KCl, 20 imidazole, 7 $MgCl_2$, 2 EGTA, and 4.6 ATP; pH 7.0). Myofibrils were then skinned for 15 min using 1% Triton X-100, centrifuged at 10,000 *g* for 5 min, and resuspended in fresh relaxing solution containing protease and phosphatase inhibitors (PhosSTOP and cOmplete ULTRA Tablets; Roche Applied Science). All samples were kept on ice until later use. Myofibrils, PKA, and all solutions were brought to room temperature (RT, 23 °C) before initiating the reaction. Myofibrils were incubated for 30 min, at 37 °C in a solution containing the catalytic subunit of bovine PKA [40] with the final concentration of PKA at 0.15 U/ug of myofibrils. Control myofibrils were incubated under the same conditions in the absence of PKA. The PKA reactions were stopped by adding Laemmli buffer and samples were heated to 90 °C for 5 min and stored in −20 °C until use for Western blots and Pro-Q/ Coomassie Brilliant Blue R-250 staining.

2.4. Determination of sarcomeric protein expression and phosphorylation levels

Western blotting and Pro-Q Diamond phosphoprotein stain (Life Technologies) were used to assess myofilament protein expression and phosphorylation in the cardiac samples as described previously [41]. Five micrograms of the solubilized myofibrils were loaded and electrophoretically separated using 4–20% Tris-glycine gels (Lonza Walkersville Inc., MD, USA) at 175 V for 90 min. For western blotting, gels were transferred to PVDF membranes and incubated overnight at 4 °C with primary antibodies (1:20000 MYBPC3 (G7) mouse monoclonal IgG1, Santa Cruz Biotechnology, sc-137237, Lot #E3116 and 1:1000 HSC 70 (B-6) mouse monoclonal IgG2a, Santa Cruz Biotechnology, sc-7298, Lot #K0217). The membranes were incubated with secondary antibodies (1:5000 goat anti-mouse IgG-HRP, Santa Cruz Biotechnology, sc-2005, Lot #A2216) for 1 h at RT, then imaged with FluorChemE Digital Darkroom system from ProteinSimple. To determine total protein phosphorylation, gels were stained with Pro-Q and imaged using GE Healthcare Typhoon Trio Variable Mode Imager System. Total phosphorylation levels of myofilament proteins were normalized to total protein expression levels which were determined by counterstaining the gels with Coomassie Brilliant Blue R-250. Coomassie gels were imaged using Azure Biosystems c600 Imaging system. Densitometric scanning of stained gels and western blots was performed using Image J software available from the U.S. National Institutes of Health, Bethesda, MD, USA [42].

2.5. Immunohistochemistry and fluorescence imaging

Immuno-fluorescent detection of cMyBPC and α-actinin was performed by confocal microscopy (Olympus Fluoview-1000) at 96× magnification on skinned myocardium isolated from NTG and $cMyBPC^{-/-}$ (KO) and virus treated KO^{WT} and KO^{Y235S} frozen heart

tissue. Skinned myofibrils were prepared by washing in fresh relaxing solution, homogenizing in rigor buffer (RB) + EGTA and RB + EGTA + 1% Triton X-100 and centrifuging at 1500 *g* for 10 min, sequentially, while resuspending the pellet in the next solution. The resuspended pellet was then incubated with gentle agitation in RB + 1% Triton X-100 for 20 min. After centrifuging at 1500 *g* for 5 min, supernatant was discarded and resuspended in RB. The solution was centrifuged again at 1500 *g* for 5 min and resuspended in RB + bovine serum albumin (BSA, 1.0 μg/μl). The solution was centrifuged and resuspended in RB + BSA 2× more, then stored at 4 °C before staining. The samples were kept on ice throughout this process. 25 μl of the samples were dispersed onto the Fisherbrand™ Fluorescent Antibody Microscope Slides with two 15 mm diameter circles and allowed to partially dry before proceeding to next stop (~15 min, RT). Slides were placed in a wet chamber for subsequent incubations at RT to prevent samples from drying out. Samples were then fixed by adding 35 μl of 4% paraformaldehyde for 10 min, washed with phosphate buffered saline (PBS) 3× (150 μl), and incubated in 50 μl of 5% goat serum for 30 min at RT. Next, 50 μl of primary antibodies (1:2000 mouse anti-MYBPC3 (G7) antibody, Santa Cruz Biotechnology, sc-137237 and 1:100 rabbit anti-actinin α antibody, Sigma-Aldrich, SAB4503474) were added directly to the goat serum and incubated at RT for 1 h. After washing with PBS 3×, 50 μl secondary antibodies (1:500 Texas RedTM goat anti-rabbit IgG (H + L), invitrogen by Thermo Fisher Scientific, REF T2767, Lot 1905916 and 1:500 Alexa FluorTM 488 goat anti-mouse IgG1 (γ1), invitrogen by Thermo Fisher Scientific, REF A21121, Lot 1820808) were added at RT for 30 min in a wet chamber. After the final wash with PBS 3×, ProLongTM Gold antifade reagent with DAPI was added as mounting media and covered with coverslips. Slides were allowed to cure overnight before being imaged with Olympus Fluoview-1000 confocal microscope using appropriate excitation and emission wavelengths.

2.6. Preparation of detergent-skinned multicellular myocardial preparations and Ca^{2+} solutions

Frozen ventricular tissue chunks were homogenized in fresh relaxing solution followed by detergent-skinning using 1% Triton-X 100 for 1 h [43]. Multicellular ventricular preparations measuring ~100 μm in width and ~400 μm in length were used for the experiments. The composition of various Ca^{2+} solutions used for the experiments was calculated using a computer program [44] and using the established stability constants [45]. Ca^{2+} solutions contained the following (in mM): 14.5 creatine phosphate, 7 EGTA, and 20 Imidazole. The maximal activating solution (pCa 4.5; pCa = $-\log [Ca^{2+}]_{free}$) also contained 65.45 KCl, 7.01 $CaCl_2$, 5.27 $MgCl_2$, and 4.81 ATP, whereas the relaxing solution (pCa 9.0) contained 72.45 KCl, 0.02 $CaCl_2$, 5.42 $MgCl_2$, and 4.76 ATP. The pH of the Ca^{2+} solutions was set to 7.0 with KOH with an ionic strength of 180 mM. A range of pCa solutions (pCa's 6.3 to 5.7), containing varying amounts of $[Ca^{2+}]_{free}$ were then prepared by mixing appropriate volumes of pCa 9.0 and 4.5 stock solutions and experiments were conducted at ~23 °C.

2.7. Experimental set up for measuring steady-state and dynamic contractile properties in skinned myocardial preparations

Detergent-skinned multicellular ventricular preparations were attached between a motor arm (312C; Aurora Scientific Inc., Aurora, Ontario, Canada) and a force transducer (403A; Aurora Scientific Inc., Aurora, Ontario, Canada), as described previously [46,47]. Changes in the motor arm position and force transducer signals were sampled at 2000 Hz using a custom-built sarcomere length (SL) control software [48]. For all mechanical measurements, the SL of the ventricular preparations was set to 2.1 μm [49]. Force-pCa relationships were determined by measuring the forces generated by the skinned myocardial preparations in a range of pCa solutions that generate submaximal to maximal forces. The apparent cooperativity of force generation was estimated from the steepness of Hill plot transformation of the force-pCa relationships [50]. The force-pCa data were fit using the eq. $P/P_o = [Ca^{2+}]^{n_H}/(k^{n_H} + [Ca^{2+}]^{n_H})$, where n_H is the Hill coefficient and k is the pCa needed to elicit half-maximal force (i.e., pCa_{50}) [51].

2.8. Stretch activation experiments to measure dynamic XB parameters

The stretch activation protocol used for this study was described in detail in previous studies [46,52]. Skinned myocardial preparations were activated in a pCa solution that generated a range of submaximal forces (~40% of maximal force at pCa 5.8). When the myocardial preparations attained a steady-state force, they were subjected to a sudden 2% stretch of their initial muscle length (ML), held at the new ML for 8 s and returned back to their initial ML. The key features of the cardiac muscle stretch activation responses have been described earlier [51]. Briefly, a sudden 2% stretch in ML causes an instantaneous spike in the force response (P1) due to a sudden strain of elastic elements within the strongly-bound XBs (Phase 1). The force then rapidly decays (Phase 2) to a minimum, due to the detachment of strained XBs into a non-force bearing state, with a dynamic rate constant k_{rel} (an index of XB detachment from actin). The lowest point of Phase 2 (nadir) is shown by P2 which is an index of the magnitude of XB detachment. Following P2, there is a gradual increase in force (Phase 3), with a dynamic rate constant k_{df} (an index of the rate of XB recruitment), which occurs due to stretch-induced recruitment of additional XBs into the force-bearing state [47]. Stretch activation amplitudes were normalized to pre-stretch steady-state Ca^{2+}-activated force as done before [46,47,51]. The magnitude of new steady-state force (P3) was measured from pre-stretch steady-state force to the peak force value attained in Phase 3, and P2 was measured from pre-stretch steady-state force to the nadir of the force response in Phase 2, whereas P_{df} was measured as the difference between P3 and P2 values [46,47,51].

k_{rel} was measured by fitting a single exponential equation to the time course of force decay using the equation: $F(t) = a(-1 + \exp.(-k_{rel}*t))$ where "a" is the amplitude of the single exponential phase and k_{rel} is the rate constant of the force decay as described earlier [46]. k_{df}, which represents the rate of recruitment of all XBs that give rise to the delayed force transient following the sudden stretch in ML, was estimated by linear transformation of the half-time of force redevelopment [46], i.e., $k_{df} = 0.693/t_{1/2}$, where $t_{1/2}$ is the time (in ms) taken from the nadir (i.e., the point of force redevelopment at the end of Phase 2) to the point of half maximal force in Phase 3 of the force response, where maximal force is indicated by a plateau region of Phase 3 (i.e., P3) [46].

2.9. Computational modeling and molecular dynamic simulation (MDS)

Multiple sequence alignment of the cardiac isoform of myosin binding protein C from 25 species was built using the NCBI Protein Database, Cluster Omega [53–55], and MView [56] and colored according to amino acid physiochemical properties described previously [57]. Template based homology modeling of PDB: 3CX2 was done using the I-TASSER server [90–92]. The homology model was validated through ProSA-web server [58] and Verify 3D [59,60] for global and local model quality. Next, the Y235S mutation was introduced in silico using the CHARMM-GUI server [61,62]. Multiple computational tools were used to calculate the change in protein stability (ΔΔG, kcal/mol) and change in thermal melting temperature (ΔT_m, K) as a result of the Y235S mutation, and the results were averaged. The following programs were used: CUPSAT [63], FoldX [64], ERIS [65], PoPMuSiC [66], STRUM [67], SDM [68], DUET [69], DynaMut [70], mCSM [71], AUTO-MUTE2.0 [72], I-Mutant [73], MUpro [74], ENCoM [75], iPTREE-STAB [76] and HoTMuSiC [77]. The wild type (WT) and the mutant (Y235S) C1 domain models were solvated with explicit TIP3P water molecules and 0.15 M KCl counter ions using Monte Carlo method in rectangular boxes (130 Å × 100 Å × 100 Å). The fully

solvated WT and Y235S models were manually checked for steric hindrances. Periodic boundary conditions were set using the Particle-mesh Ewald (PME) method, and short steps of minimization were performed to remove bad contacts using the CHARMM-GUI platform. MolProbity [78,79] was used to validate and confirm all atom contacts and geometry before the simulation. The simulation time step was set to 2.0 fs and coordinates were saved every 20 ps. After a 100 ps minimization under the NVT ensemble, the system was equilibrated and simulated for 500 ns under the NPT ensemble at 296.15 K and 1.0 atm with Langevin dynamics/piston method using NAMD 2.10 [80] and CHARMM36m force field [81]. Three simulation trials (total of 1.5 μs) were done for both WT and Y235S groups. The root mean square deviation (RMSD), root mean square fluctuations (RMSF), total hydrogen bonds, salt bridges, secondary structure, solvent accessible surface area (SASA), and radius of gyration were all analyzed using VMD (University of Illinois at Urbana-Champaign, Champaign, IL, USA) [82–84] after the completion of MDS. Using the last frame of the 500 ns simulation, electrostatic potential maps were created using PDB2PQR [85] server and VMD Plugin APBS Electrostatics [86] and hydrogen bonding interactions using Residue Interaction Network Generator (RING2.0) software [87]. The representative domain conformation, intramolecular networks, and electrostatic potentials were visualized with VMD, The PyMOL Molecular Graphics System, Version 2.1 Schrödinger, LLC., and Dassault Systèmes BIOVIA Discovery Studio 2018.

2.10. Data analysis

Skinned fiber mechanical data were analyzed as previously described [41]. Comparisons of in vitro measurements between groups were performed using a one-way analysis of variance (ANOVA) followed by a Tukey-Kramer post hoc test. Comparisons of protein expression and phosphorylation with or without PKA treatments were performed using Student's *t*-test as appropriate. Values are reported as mean ± standard error of mean (S.E.M.) and the criterion for statistical significance was set at $P < 0.05$. Modeling and MDS data were analyzed using VMD, PyMOL, and Discovery Studio. Values of all simulation data are presented as combined mean ± standard deviation (S.D.). Student's *t*-test was used and statistical significance was set at $P < 0.05$. All graphs were made using GraphPad Prism Software version 6.01, La Jolla California USA, www.graphpad.com.

3. Results

3.1. Sarcomeric protein expression and phosphorylation

Western blotting and Pro-Q phospho-staining were done on non-transgenic (NTG) wild-type myocardium, myocardium lacking cMyBPC (KO), and KO myocardium injected with WT (KO^{WT}) and Y235S (KO^{Y235S}) constructs. Western blots showed no significant differences in cMyBPC expression among NTG, KO^{WT}, and KO^{Y235S} groups (Fig. 2(a)). As expected, cMyBPC was absent in KO samples. Pro-Q phospho-stain showed no significant differences in total phosphorylation of cMyBPC, cardiac troponin T (cTnT), and cardiac troponin I (cTnI) among all samples prior to PKA treatment (Fig. 2(b)). Following PKA treatment, phosphorylation levels of cMyBPC and cTnI increased, and there were no differences in phosphorylation levels of KO^{WT} and KO^{Y235S} myocardium.

3.2. Immunohistochemistry and cMyBPC localization

Proper sarcomeric localization of cMyBPC (doublets) in the C zone and α-actinin in the Z disc (singlets) was confirmed in the KO^{WT} and KO^{Y235S} groups by immunohistochemistry as depicted in Fig. 3. As expected, cMyBPC was absent in the KO group (Fig. 3).

3.3. Effect of Y235S mutation on myofilament Ca^{2+} sensitivity (pCa_{50}) and cooperativity of force development (n_H)

All four experimental groups, NTG, KO, KO^{WT}, and KO^{Y235S} showed similar force generation at Ca^{2+}-independent and maximal Ca^{2+}-activated states (Table 1). Compared to the KO^{WT} group, the KO^{Y235S} group showed a significantly increased pCa_{50} (5.82 ± 0.02 for KO^{WT} vs. 5.89 ± 0.02 for KO^{Y235S}; $P < 0.05$) (Table 1) as demonstrated by a significant left-ward shift in the force-pCa relationship of KO^{WT} and KO^{Y235S} myocardium (Fig. 4). However, the increase in force generation primarily occurred at forces < ~50% of maximal force (Fig. 4). The Hill coefficient, n_H, for KO^{Y235S} was decreased compared to KO^{WT} group (3.81 ± 0.33 for KO^{WT} vs. 3.14 ± 0.31 for KO^{Y235S}; $P < 0.05$), consistent with enhanced force generation at submaximal Ca^{2+}-activations (Table 1).

3.4. The effect of Y235S mutation on dynamic stretch activation parameters

The impact of the Y235S mutation on the rate of XB detachment was assessed by measuring k_{rel} [88]. Our results show that the KO^{Y235S} myocardium displayed accelerated k_{rel} (~31%; $P < 0.05$) and a greater magnitude of XB detachment (0.031 ± 0.012 for KO^{WT} vs. −0.008 ± 0.015 for KO^{Y235S}; $P < 0.05$) compared to the KO^{WT} myocardium (Table 2).

The impact of the Y235S mutation on the rate and magnitude of XB recruitment was assessed by measuring k_{df} and P_{df}, respectively [88]. The rate of XB recruitment (k_{df}) of the KO^{WT} myocardium was 6.36 ± 0.41 s^{-1}, whereas k_{df} in the KO^{Y235S} myocardium was 8.11 ± 0.43 s^{-1} (~28% increase; $P < 0.05$, Table 2). The magnitude of XB recruitment (P_{df}) was also significantly greater in the KO^{Y235S} myocardium compared to the KO^{WT} myocardium (0.249 ± 0.017 for KO^{Y235S} vs. 0.195 ± 0.013 for KO^{WT}; $P < 0.05$) (Table 2). Despite these differences, the Y235S mutation did not affect the new steady-state force attained after the imposed stretch (i.e. P3) compared to KO^{WT} (Table 2). As expected, a complete lack of cMyBPC in the KO group exacerbated the acceleration in k_{rel} and k_{df}, as well as increased magnitudes of XB detachment (P2) and recruitment (P_{df}) (Table 2).

3.5. Template-based homology modeling and molecular dynamics simulations (MDS)

Currently, there are four 3D structures of C1 domain from X-ray crystallography and NMR spectroscopy studies in the Protein Data Bank (PDB: 2V6H [38], 3CX2 [89], 2AVG [31] and 4EDQ (to be published)). The best resolution X-ray crystallography structure of a human C1 domain of cMyBPC (PDB: 3CX2, resolution = 1.3 Å, residues 151–258 in human sequence) was chosen for our computational studies. Combining the structure of 3CX2 and the sequence of *Mus musculus* (UniProtKB, O70468) in I-TASSER [90] server, a template-based homology model of mouse-specific C1 domain was created (residues 149–256 in mouse sequence, 91.6% sequence identity). The original WT model had a C-score [91] of 0.98 and expected TM score [92] of 0.85 ± 0.08 (Fig. 5(a)). ProSA-web server results showed that the homology model was of good overall and local model quality (Z-score = − 4.81). Next, Verify 3D showed that 94.44% of the residues had averaged 3D-1D score ≥ 0.2, implying good compatibility of the model (3D) with its amino acid sequence (1D). Using the original WT model, both the WT and Y235S models were prepared in CHARMM-GUI [61,62]. The fully solvated WT and Y235S systems contained 122,690 and 122,632 atoms, respectively, with proper ionic strength, temperature and periodic boundary conditions. After a 100 ps minimization, MolProbity showed that there was an acceptable range of all atom contacts and geometry with an overall MolProbity score of 1.39 (97th percentile). Using the same models, three trials of 500 ns MDS were performed for both WT and Y235S.

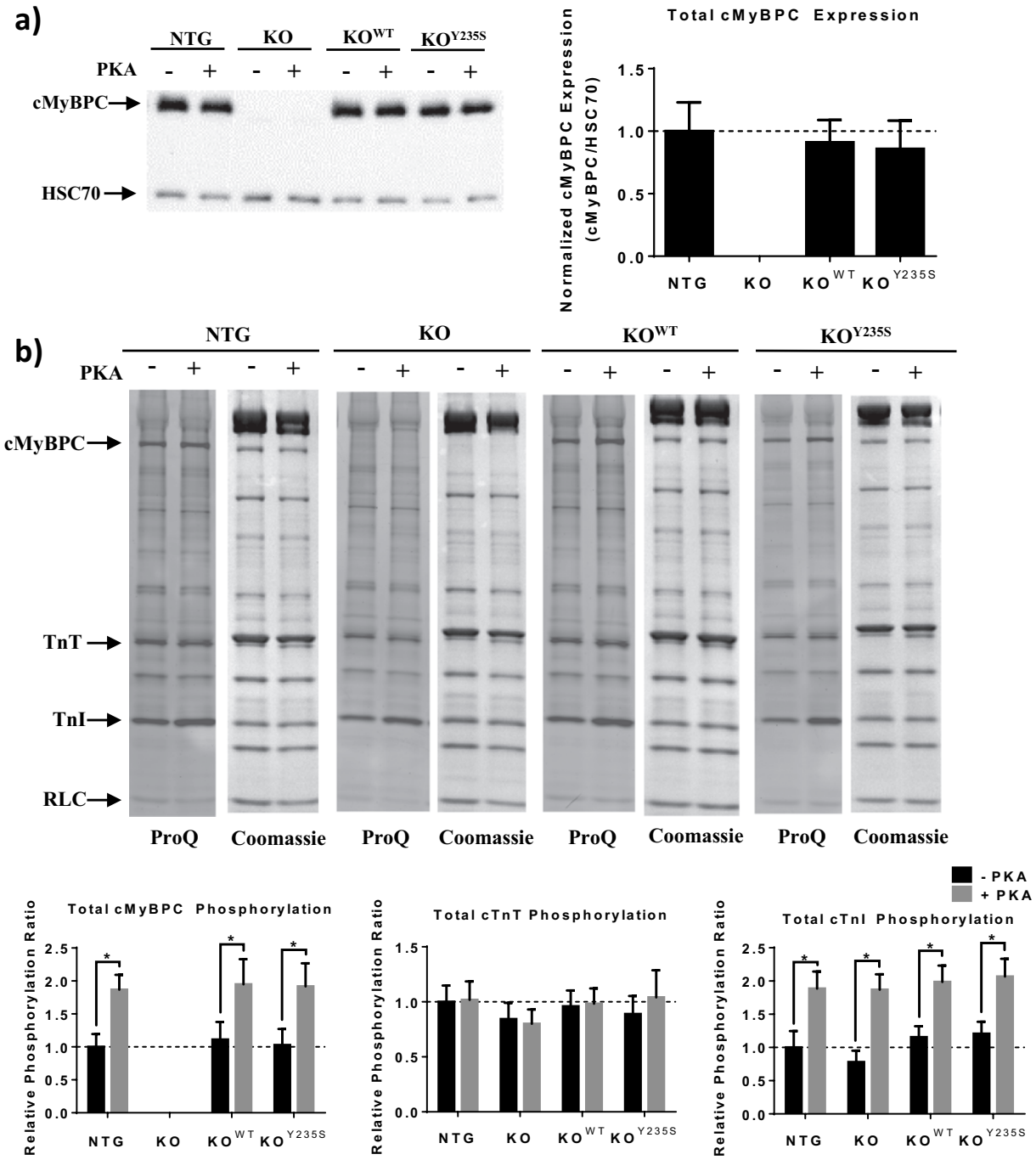

Fig. 2. Determination of protein expression and PKA-mediated phosphorylation of cMyBPC and other sarcomeric proteins. **(a)** Representative Western blot and quantification of cMyBPC showing total protein expression. **(b)** Representative gels shown are stained by Pro-Q (left) for total protein phosphorylation, and the same gel is shown for total protein level (right) stained with Coomassie Brilliant Blue. Relative protein phosphorylation (phosphorylated signal/total protein signal) was calculated for each protein and is expressed as % of NTG -PKA values for that protein. Values are expressed as mean ± S.E.M., from four hearts in each group. *$P < 0.05$, different from non-PKA-treated samples from the same group.

3.6. The stability of the WT and Y235S C1 domain models

Various bioinformatics tools were utilized to calculate the change in C1 domain stability upon Y235S mutation; all methods predicted Y235S to be destabilizing, with an average ΔΔG value of −2.81 ± 0.46 kcal/mol. In addition, the simulated change in melting temperature from WT to Y235S was consistently predicted to be less stable, with a value of $\Delta T_m = -7.65 \pm 2.09$ K. After each trial of the 500 ns production runs, the average RMSD were calculated for WT and Y235S models (2.75 ± 0.31 Å and 2.89 ± 0.35 Å, respectively; $P = 0.16$) and both models stabilized to about 3 Å after 10 ns, with no sign of unfolding (Fig. 5(b)). The RMSD Gaussian plot showed that both the WT and Y235S structures were normally distributed and the two systems were well equilibrated with no evidence of unfolding (Fig. 5(b)). The average RMSF per residue showed little differences across most residues. However, the Y235S model residues W189-K191, L207, H223, T229-S231, S235, F250, and L252-V254 showed increased RMSF values compared to the WT model ($P < 0.05$); interestingly, they were all located in the C-terminal end of C1 domain (shaded and marked with asterisks in Fig. 5(c)). H204, located in the body of the C1 domain, was

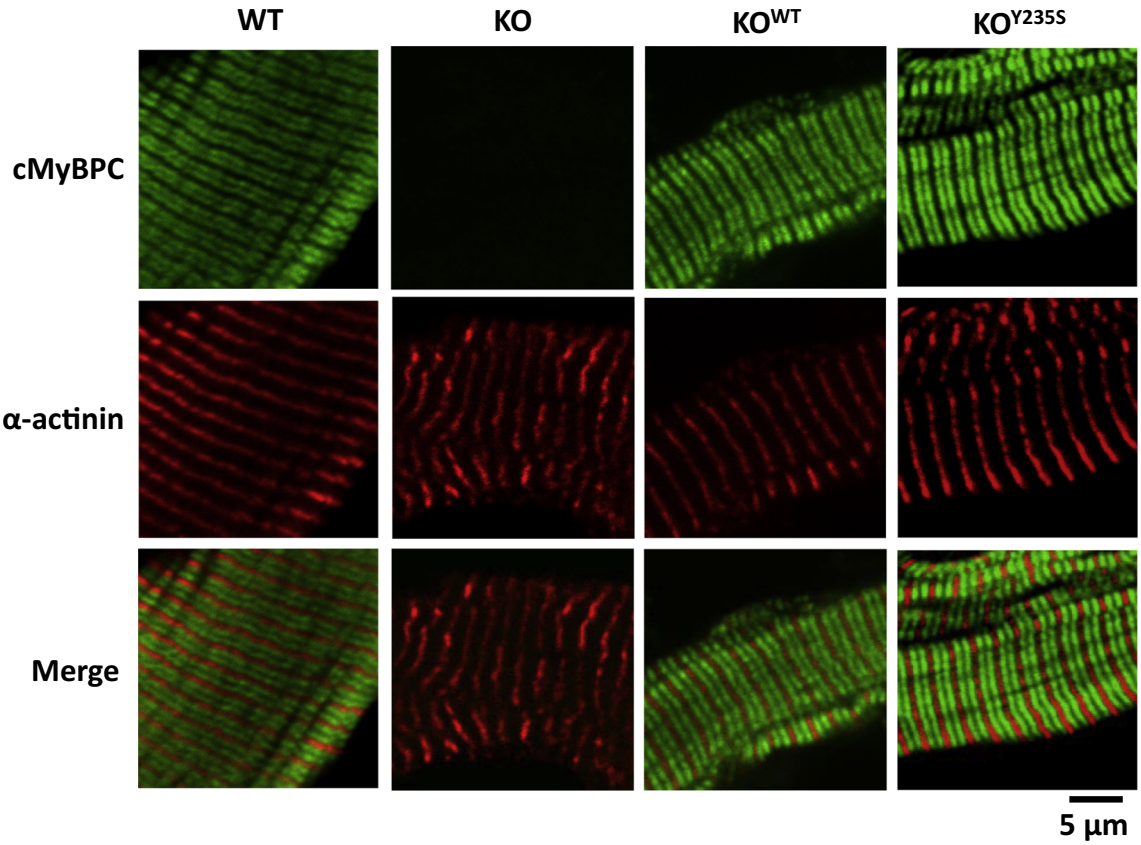

Fig. 3. Immunohistochemical analysis. Confocal microscopy (×96 magnification) was used to demonstrate the localization of α-actinin (red) and cMyBPC (green) in non-transgenic (NTG), cMyBPC $^{-/-}$ (KO), and cMyBPC$^{-/-}$ myocardium treated with lentiviruses encoding the wild type cMyBPC (KO^{WT}) and Y235S mutant cMyBPC (KO^{Y235S}). Scale bar: 5 μm.

Table 1
Steady-state contractile parameters measured in NTG, KO, KO^{WT}, and KO^{Y235S} detergent-skinned myocardium.

Group	F_{min} (mN/mm^2)	F_{max} (mN/mm^2)	n_H	pCa_{50}
NTG	1.04 ± 0.10	17.84 ± 1.67	3.69 ± 0.26	5.83 ± 0.01
KO	0.89 ± 0.19	19.44 ± 1.57	3.28 ± 0.27*	5.87 ± 0.01*
KO^{WT}	0.94 ± 0.12	18.91 ± 1.93	3.81 ± 0.33	5.82 ± 0.02
KO^{Y235S}	0.97 ± 0.14	18.12 ± 1.78	3.14 ± 0.31*	5.89 ± 0.02*

F_{min}, Ca^{2+}-independent force measured at pCa 9.0; F_{max}, Ca^{2+}-activated maximal force measured at pCa 4.5; n_H, Hill coefficient of the force-pCa relationship; pCa_{50}, pCa required for the generation of half-maximal force. Values are expressed as mean ± S.E.M.

* Significantly different compared to KO^{WT}; $P < 0.05$.

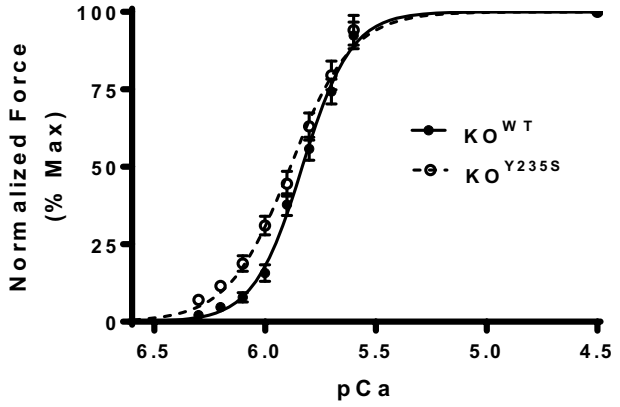

Fig. 4. Force-pCa relationship between KO^{WT} and KO^{Y235S} myocardium. The KO^{Y235S} myocardium shows a left-ward shift in the pCa curve, indicating increased calcium sensitivity. A total of 15 skinned myocardial preparations (3 fibers each from 5 hearts) were used for both groups. Values are expressed as mean ± S.E.M.

the only residue that had decreased RMSF compared to the WT structure ($P < 0.05$, Fig. 5(c)). Overall, the Y235S mutation may have caused localized destabilization by increasing the fluctuations of select residues involved in specific intramolecular interactions, especially in the C-terminal end of the C1 domain.

3.7. The Y235S model shows disrupted hydrogen bonding chain

The average number of hydrogen bonds in the WT simulations were significantly different from the Y235S simulations (27.13 ± 4.09 vs. 25.64 ± 4.05; $P = 0.001$). In the WT C1 domain, Y235 seemed to be a part of a large hydrogen bonding network, stretching from G167, G168, D226, and A227 to Q228, S231, Y235 and F250 (Fig. 6(a)). For the mutant C1 domain containing S235, there was a general rearrangement and reshuffling of hydrogen bonding patterns localized in the C-terminal loops and the BDE β-sheets (see Fig. 1 for β-sheet nomenclature and Fig. 5(a) for positions of β-sheets in the C1 domain). More specifically, Y235 participated in a hydrogen bond with S231 in the WT model, as shown in Fig. 6(a). However, the tyrosine to serine mutation at residue 235 replaced a long amino acid side chain to a small and short hydroxyl group. Therefore, the mutation abolished the connection between residues Y235 and S231, causing the hydrogen bonding network of G167, G168, D226, and Q228 to be isolated from the rest of the 7 residue network mentioned above (Fig. 6(b)).

Table 2
Dynamic stretch-activation parameters measured in NTG, KO, KO^{WT}, and KO^{Y235S} detergent-skinned myocardium.

Group	P1 ($P1/P_o$)	P2 ($P2/P_o$)	P3 ($P3/P_o$)	P_{df}	k_{rel} (s^{-1})	k_{df} (s^{-1})
NTG	0.615 ± 0.019	0.028 ± 0.009	0.233 ± 0.017	0.205 ± 0.014	511 ± 22	6.04 ± 0.39
KO	0.502 ± 0.012*	−0.039 ± 0.012*	0.269 ± 0.026	0.308 ± 0.018*	813 ± 35*	10.27 ± 0.49*
KO^{WT}	0.597 ± 0.016	0.031 ± 0.012	0.226 ± 0.015	0.195 ± 0.013	502 ± 27	6.36 ± 0.41
KO^{Y235S}	0.546 ± 0.018*,#	−0.008 ± 0.015*,#	0.241 ± 0.019	0.249 ± 0.017*,#	657 ± 32*,#	8.11 ± 0.43*,#

P1, XB stiffness; P2, magnitude of XB detachment; P3, the new steady-state force attained in response to the imposed stretch in muscle length; P_{df}, magnitude of XB recruitment; P_o, pre-stretch isometric force; k_{rel}, rate of XB detachment; k_{df}, rate of XB recruitment. Values are expressed as mean ± S.E.M.
* Significantly different compared to KO^{WT}; $P < 0.05$.
# Significantly different compared to KO; $P < 0.05$.

3.8. Hydrophobic interactions in the core of C1 domain

In the WT C1 domain, Y235 had multiple direct hydrophobic and pi-pi stacking interactions with residues F172, I224, F250, and L252 (Fig. 6(c)). The web of hydrophobic interactions created by Y235 extended to A227, L222 and W189, all contributing to the energetically favorable hydrophobic core formation (Fig. 6(c)). However, in the Y235S mutant model, S235 did not form any direct side chain-mediated hydrophobic or pi-pi stacking interactions, and many interactions were abolished (Fig. 6(d)). Some specific hydrophobic interactions were abolished, such as with L252-I224 or F172-L222, and as a result, the core was less stable and generally had a less compact volume based on the average distance of hydrophobic bonds that remained (Fig. 6(d)). The alterations in the atomic positions of these residues may propagate their effect to the rest of the domain and cause changes in surface conformation of the domain.

3.9. Ionic interaction pairs and salt bridges may affect domain structure and stability

In addition to interactions in the core of the domain, there were altered salt bridge occupancies on the outside, possibly as a result of the Y235S mutation. We observed that the average occupancy of the salt bridge pair K188-D196 is 53.78% in the WT vs. 64.41% in the Y235S model ($P = 0.19$, Fig. 7). Strengthening this ionic interaction may change the position of the CD loop, altering the surface interface in the C-terminal end of the mutant C1 domain. In contrast, the Y235S mutation also caused slight decrease in occupancies of salt bridge pairs R236-E238 and R158-D246 (Fig. 7), although statistical significance was not found. Given their positions in the C1 domain, we postulated that the Y235S mutation may have caused some destabilization that propagated to sites not directly next to the mutation. Ionic interactions give substantial binding/ stabilization energy to the C1 domain, but when altered, the domain structure and surface charges can be interrupted, potentially leading to functional changes seen in the fiber kinetic study.

3.10. Secondary structure of the Y235S model is unchanged compared to the WT model

By plotting secondary structure assignments in the entire 500 ns trajectory for every residue, we were able to observe how secondary structure elements changed with time. Because secondary structure is primarily determined by the backbone residues, which are identical between tyrosine and serine, we expected to see no significant differences. Indeed, both Y235 and S235 residue backbones participated in β-sheet stabilization through F250 hydrogen bond interactions, so the secondary structure of C1 was not dramatically altered by the Y235S mutation (Fig. 8). But interestingly, residues T229 to G233 in the C-terminal end of C1 domain changed permanently to a disorganized random coil from an alpha helix (Fig. 8). Additionally, residues F250 to L252 were converted from an extended conformation β-sheet to a random coil in the Y235S mutant model (Fig. 8).

3.11. Conformational and surface properties of WT and Y235S C1 domains

The Y235S model did not show statistically significant difference in radius of gyration compared to the WT model (WT 14.75 ± 0.09 Å vs. Y235S 14.76 ± 0.11 Å; $P = 0.903$), indicating that the Y235S mutation did not cause any significant changes to the degree of C1 domain compaction. Based on surface inspection and analyses, the WT C1 domain showed a relatively flat and smooth surface on the N-terminal end of the C1 domain, below the CD loop. However, the mutant C1 domain showed a bumpy solvent accessible surface with deep ridges and grooves at the N-terminal end due to CD and EF loop movement (likely due to the change in side chain size). In fact, SASA for residue 235 changed from 337.25 ± 4.27 $Å^2$ to 217.77 ± 3.29 $Å^2$ due to the mutation ($P < 0.05$, Fig. 9(a)). As a result, the solvent accessible surface near S235 became more irregular with deep grooves compared to the WT (Fig. 10(a)). It also had a significantly deep solvent accessible bulge taking up volume within the hydrophobic core of the C1 domain, where a bulky tyrosine residue was mutated to a smaller serine residue (Fig. 9(b)). Since structural protein function is impacted by solvent accessible area and surface conformation, the above mutational changes may have negative effects on proper C1 domain function.

3.12. Changes in the electrostatic potential maps of WT and Y235S models

The Y235S mutation model also displayed an altered electrostatic surface in the C-terminal end of C1 domain (Fig. 10(a)). It showed a slight increase in the positively charged surface area (blue) and a general reduction in the amount of charges on the surface of the C-terminal end (Fig. 10(a)). The electric isocontour and field lines of the Y235S model showed similar results, including a general increase in the magnitude of positively charged residues shown by a larger isocontour volume (Fig. 10(b)) and an increase in electric field lines throughout the outer perimeter of the C-terminal end (Fig. 10(c)). Both panels for Y235S exhibited disorganization of charge distributions. These changes in electrostatic potential and charge distributions may contribute to altered interactions with myosin or actin as reported in previous studies [93–95].

4. Discussion

Although cMyBPC mutations are a leading cause of HCM, the molecular mechanisms of its mutations are still unclear. Available data show that around 50% of MYBPC3 mutations result in truncated protein products [96,97], while the rest result in insertion/deletions, frameshifts, or single amino acid missense mutations [35]. It has been suggested that some truncated proteins may act as dominant negative poison poly-peptides [17], while other studies have suggested that haploinsufficiency is the main mechanism of disease [98]. In a clinical study of missense mutations of MYBPC3, the total protein expression was reduced, which suggested that some missense variants may increase the susceptibility to degradation through nonsense mediated mRNA decay, ubiquitin mediated proteolysis, and other pathways [99,100]. More recent studies have shown that MYBPC3 missense

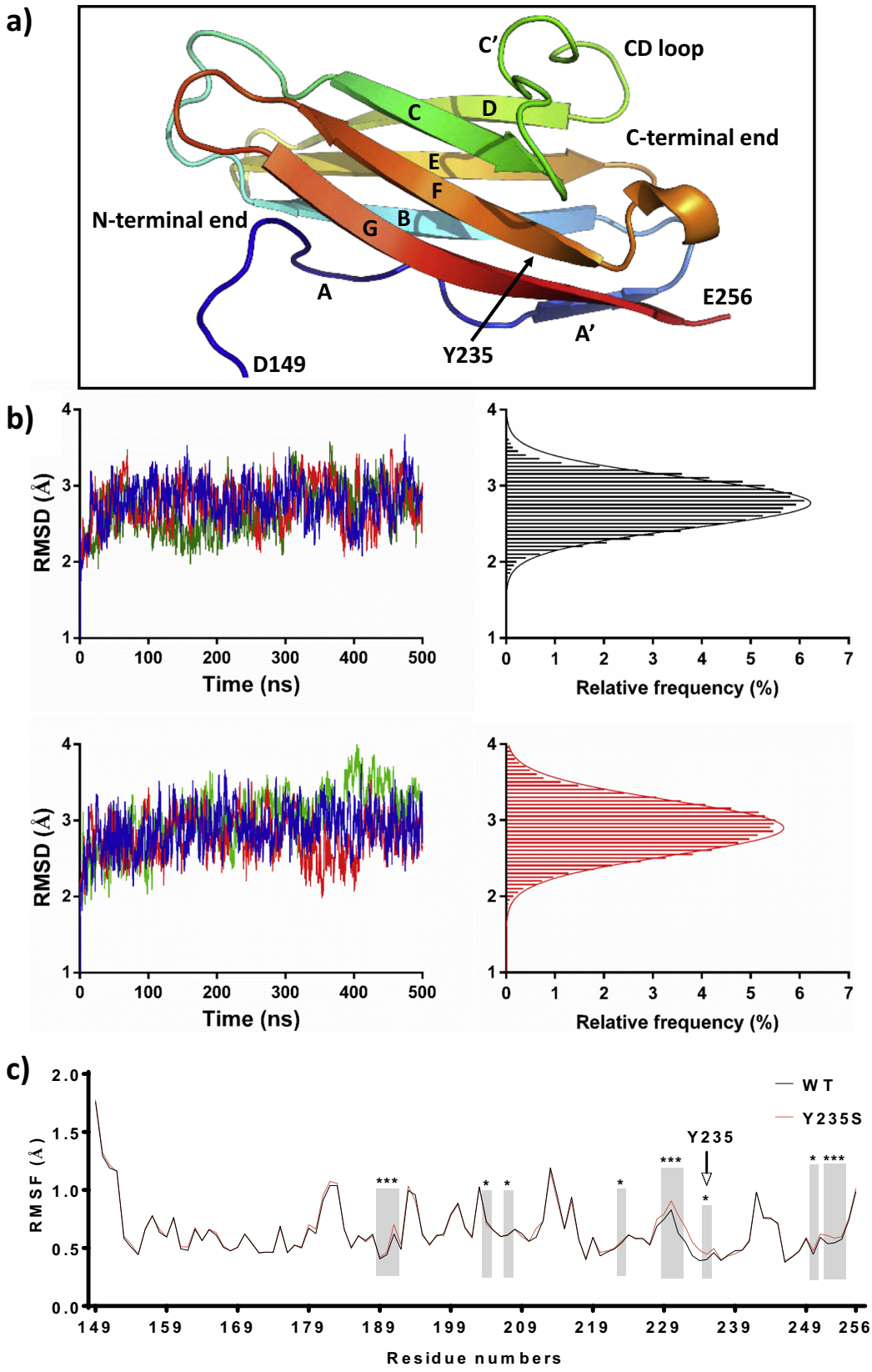

Fig. 5. Structural parameters of the C1 domain. **(a)** Representative cartoon structure of mouse C1 domain template-based homology model created using the 3CX2 X-ray crystallographic structure. The first and last residue of the domain, N- and C-terminal ends, secondary structure nomenclature and residue Y235 of the C1 domain are shown. PyMOL was used to render the image. **(b)** 500 ns RMSD trajectory plot and Gaussian distribution of wild type (WT) and mutant (Y235S) C1 domain homology model of mouse cMyBPC. Only hydrogen atoms were excluded from the RMSD calculation. MDS of both models show gradual equilibration and stabilization to about 3.0 Å. The structures were stable until the end of the simulation. Various RMSD peaks indicate natural fluctuations due to sidechain movements. **(c)** Averaged RMSF per residue of C1 domain. Highlighted residues are statistically significant. Values are expressed as mean ± S.D.; $^{*}P < 0.05$. VMD was used to obtain data and render the image.

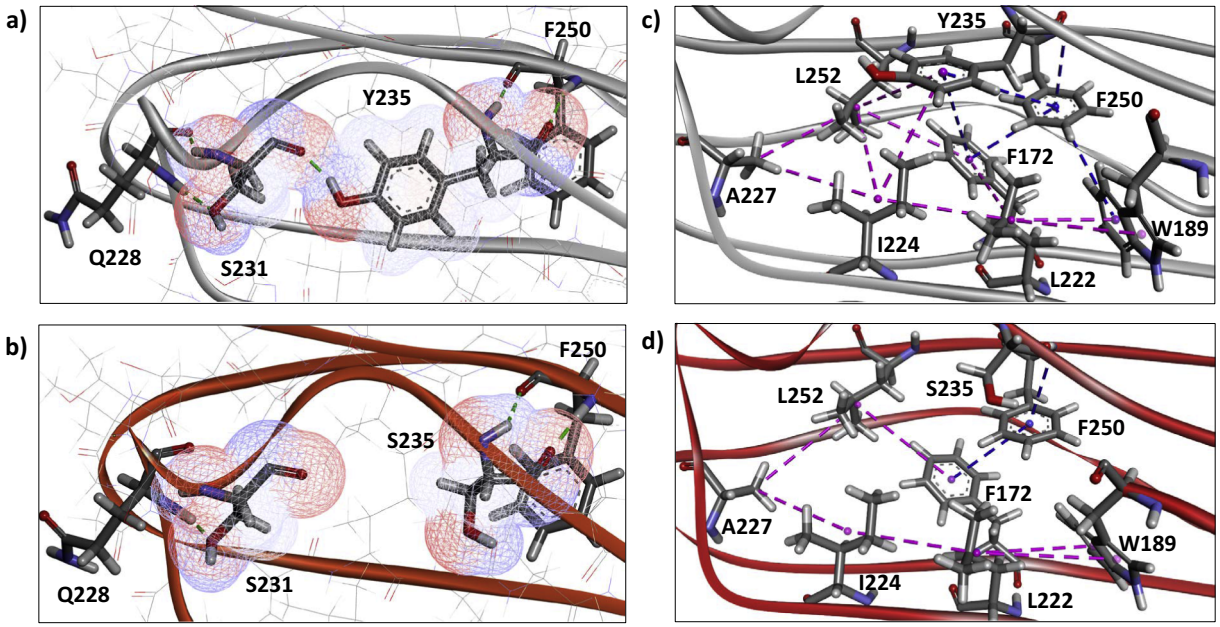

Fig. 6. Representative intramolecular hydrogen bond and hydrophobic interactions. WT and Y235S models are shown in gray and red cartoon representations, respectively. Hydrogen bonding interactions of Y235 in **(a)** WT and **(b)** Y235S models are shown. The connection between S235 and S231 is broken in the Y235S mutant model. The VDW radius of those two residues are also shown as a wire mesh, colored by atom charge. Green dashes indicate conventional hydrogen bonds (distance threshold = 2.5 Å). The intricate networks of hydrophobic interactions are represented in **(c)** WT and **(d)** Y235S models. It is zoomed into the hydrophobic core of the C1 domain. Key residues are shown as stick figures. Pink dashes indicate alkyl-alkyl or pi-alkyl hydrophobic interactions (distance threshold = 0.5 Å of van der Waals radii) and blue dashes indicate pi-pi or amide-pi stacking interactions (distance threshold = 6.5 Å). Distance measurements defined by RING2.0 software were used. Many of the core-stabilizing interactions are ablated in the Y235S model. Discovery Studio was used to render the images.

mutations produced full length mutant proteins; some seem to lead to haploinsufficiency [98,101,102], while others did not [103]. There is evidence that truncated proteins may cause disease directly through haploinsufficiency or indirectly by inducing cytotoxicity or disrupting myofibrillar architecture [98]. Therefore, the pathologic mechanism of missense mutations is thought to be heterogeneous based on the degree of structural stability and is unique to alterations specific to the mutation in the protein. In this study, we characterized the mechanism by which the pathogenic MYBPC3 Y235S missense mutation caused contractile dysfunction by performing mechanical experiments on skinned myocardium isolated from cMyBPC null mouse hearts following in vivo viral transfection of wild-type or Y235S MYBPC3. To probe the molecular mechanisms underlying mechanical dysfunction due to mutant Y235S cMyBPC expression, we performed in silico computational studies and MDS to determine its impact on C1 domain structure.

In our study, we showed that the introduction of Y235S missense mutation through lentiviral-mediated gene transfer did not induce significant changes in protein expression or phosphorylation levels of cMyBPC and other sarcomeric proteins (Fig. 2(a) and 2(b)). In addition, the expression of mutant Y235S cMyBPC resulted in hypercontractile XB behavior that was intermediate to the WT myocardium and myocardium lacking cMyBPC, with accelerated rates of XB recruitment and relaxation kinetics and enhanced Ca^{2+} sensitivity of force generation (Table 2). Furthermore, immunohistochemistry showed normal expression levels of transduced Y235S mutant cMyBPC that also localized correctly into C zones without evidence of accumulation of degraded protein products (Fig. 3). Therefore, our data indicate that the Y235S mutation exerts hypercontractility through a direct effect of Y235S on myofilament function and XB behavior, rather than via mechanisms involving poison poly-peptide or haploinsufficiency.

Results from thermal melting simulation and computational stability predictions showed that the introduction of Y235S causes a moderately destabilizing effect ($\Delta\Delta G = -2.81 \pm 0.46$ kcal/mol and $\Delta T_m = -7.65 \pm 2.09$ K). The reduction in ΔT_m also indicates that the Y235S mutation decreased the stability of C1 domain by reducing the amount of thermal energy required to denature the mutant Y235S C1 domain structure. Previous research has shown that mutations that reduce ΔΔG by greater than about 1–3 kcal/mol are destabilizing and may cause severe disease phenotypes [104,105]. Taken together, the Y235S mutation reduces ΔΔG and ΔT_m to intermediate values, which may not cause severe disease phenotypes. In fact, our MDS results showed that Y235S did not completely unfold the C1 domain and caused only an intermediate change in dynamic stretch-activation kinetic properties compared to a complete ablation of cMyBPC in the KO model (Table 2). The moderate destabilizing effect of Y235S may also explain the proper sarcomeric expression and localization of the mutant Y235S cMyBPC proteins (Fig. 3).

The accelerated XB recruitment rate (k_{df}) seen in the fiber kinetic experiments may be attributable to alterations in the interaction between cMyBPC and myosin sub fragment 2 (myosin S2). Previous studies have found that the C-terminal end of the C1 domain, where residue 235 is located, has been shown to be important in interacting with myosin S2 [31,106]. The study of Ababou et al. [31] showed that the positions of the following cMyBPC residues in C1 domain were perturbed above $< \Delta\delta >_{tot} + 1*\sigma$ (ppm) in NMR titration experiments of ^{15}N-labeled C1 domain with S2Δ: G192, K193, W194, V195, L197, V201, Q203, H204, H223 (F233 in the human sequence), T225, D226, Q228, H255, and E256 [31]. Our MD simulation data showed that the introduction of Y235S mutation destroyed the hydrogen bonding network of G167, G168, D226, A227, Q228, S231, Y235 and F250, in this order (Fig. 6(a) and 6(b)). The hydrogen bond between S231 and Y235 was broken as a result of the mutation, and the atomic positions of D226 and Q228 were changed. Altered Q228 hydrogen bonding position may thus have a role in altered myosin S2 binding. This separation event may propagate to further rearrangements of hydrogen bond networks in both the N- and C-terminal ends of C1 domain, including the CD loop. The Y235S mutation also changed the mutant C1 domain's C-terminal end surface conformation and electrostatic charge. In fact, the probable myosin S2 binding region of the C-terminal end of C1 domain was shown to be negatively charged (highly acidic) [31,38];

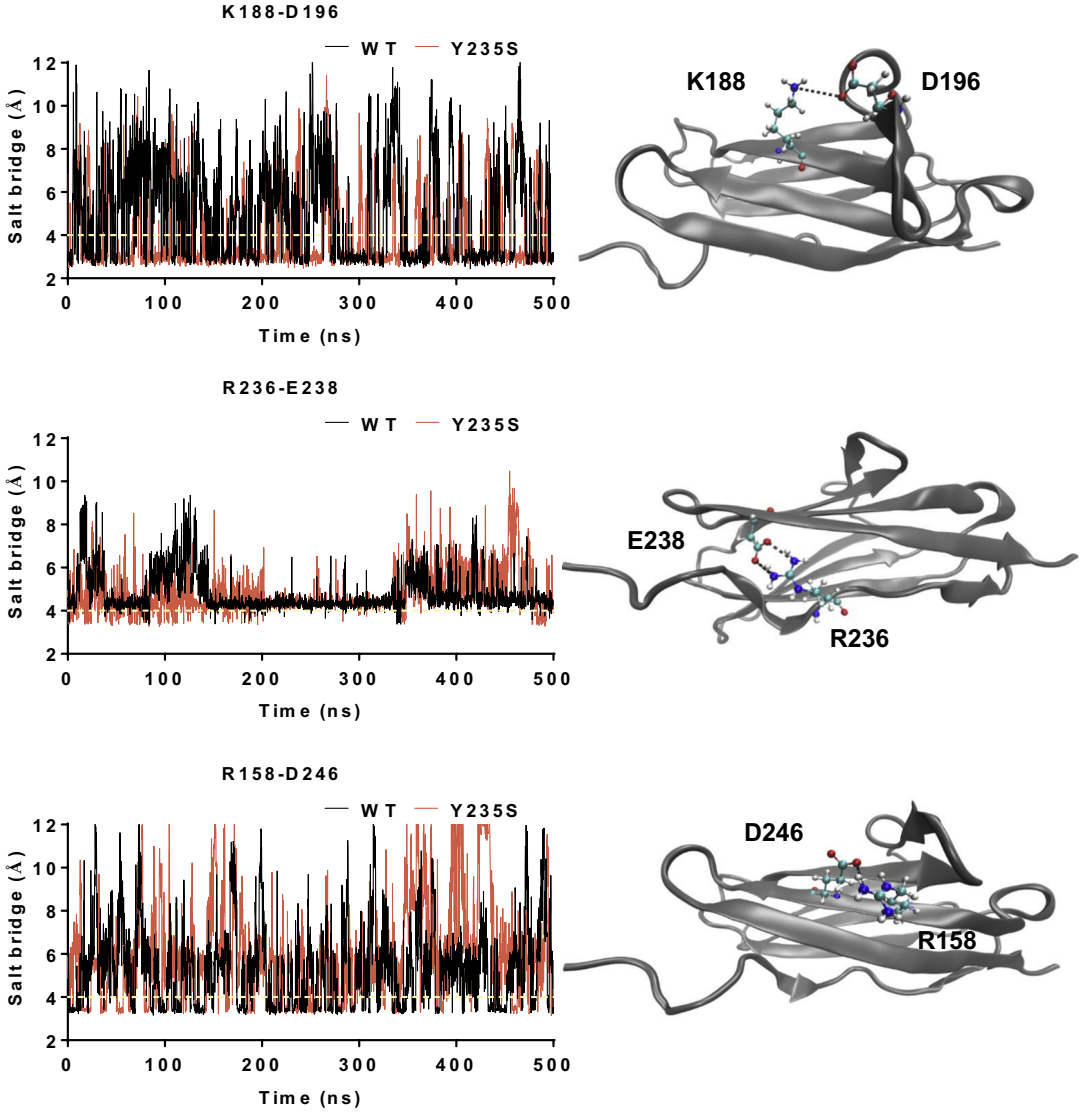

Fig. 7. Three representative intramolecular salt bridge trajectory plots for K188-D196, R236-E238, and R158-D246. The left panels show combined WT and Y235S trajectory plots of salt bridge bond distance vs. time. The dotted yellow lines at 4 Å indicate the upper boundary of salt bridge formation. The right panels show the 3D positions of the above salt bridges K188-D196, R236-E238, and R158-D246. The residues are labeled and colored in CPK using VMD.

however, the electrostatic surface of the mutant Y235S C1 domain's C-terminal becomes much more positive (Fig. 10). In addition, the RMSF of myosin binding residues H204 ($P = 0.022$) and H233 ($P = 0.050$) were significantly altered, possibly increasing fluctuations in the interaction interface. Collectively, it is possible that the above changes may disrupt proper cMyBPC binding with myosin S2.

The enhanced XB recruitment rate (k_{df}) in fiber kinetic experiments of KO^{Y235S} myocardium may also be attributable to alterations in the interaction between cMyBPC and myosin sub fragment 1 (myosin S1). A recent microscale thermophoresis (MST) experiment showed that the C1 domain may have a role in binding to myosin S1 and the myosin mesa, such that cMyBPC sequesters myosin S1 into a nonfunctional state whereas this inhibition is relieved upon phosphorylation of cMyBPC [23]. Since S1 and the myosin mesa are heavily charged, the Y235 mutation-induced changes in surface charge may weaken the intermolecular interactions of cMyBPC with S1 (Fig. 10). Thus, the inability of cMyBPC to hold the myosin head in an inactive form may be another potential mechanism that led to an accelerated XB recruitment as shown by our skinned fiber data (Table 2). These apparent surface charge alterations as well as the local disorganization, increased fluctuations, and changed binding partner positions/interactions may all lead to aberrant cMyBPC-myosin S1 and S2 interactions. As a result, myosin heads are less restricted by cMyBPC allowing enhanced thin filament binding, thereby accelerating the rates of XB recruitment.

We also observed that the expression of Y235S mutant cMyBPC accelerated the rate of XB detachment rate (k_{rel}) and increased the magnitude of XB detachment (P2) compared to KO^{WT}. A previous NMR titration experiment using a cMyBPC fragment and G-actin showed that some C-terminal residues, including W189, V195, D196, K200, Q228, Y235, and S240, may be important in interacting with actin because those residues were perturbed above $< \Delta\delta >_{tot} + 1*\sigma$ (ppm) upon binding to actin [32]. As explained earlier, Q228 participates in a hydrogen bond network that was broken when tyrosine residue 235 was mutated to serine, with associated displacement of the Q228 atoms (Fig. 6(b)). In the intramolecular analysis of hydrophobic and pi-pi interactions, both W189 and Y235 were vital for proper hydrophobic core formation (Fig. 6(c) and 6(d)). The Y235S mutation causesd dissociation of many important hydrophobic bonds, and causesd peripheral residues to move away from the core. In addition, D196, an important residue for actin binding, participated in an ionic bond with K188 that was stabilized in the Y235S model (Fig. 7(a)). The increased occupancy of this pair of salt bridge may cause the CD loop to fold back towards

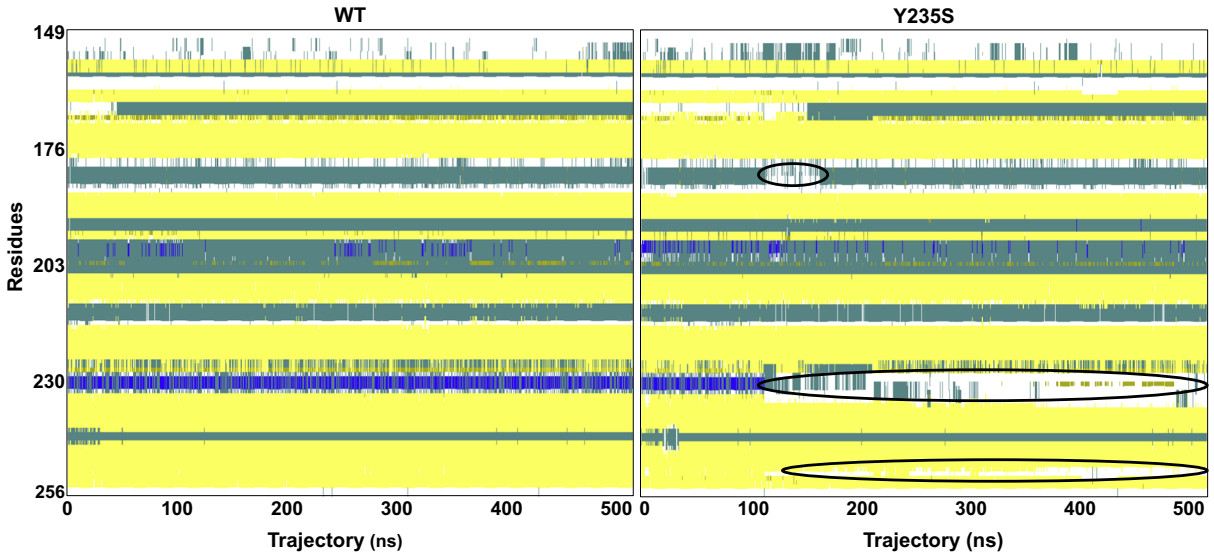

Fig. 8. Secondary structure profile. A sample secondary structure per residue (spanning residues D149 to E256) for the whole 500 ns trajectory graphed in VMD plug-in Timeline, with DSSP classification of secondary structure of WT (left) and Y235S (right). The black ovals show transient changes as well as changes in residues T229 to G233 and F250 to L252 in the Y235S model. VMD was used to obtain data and render the image.

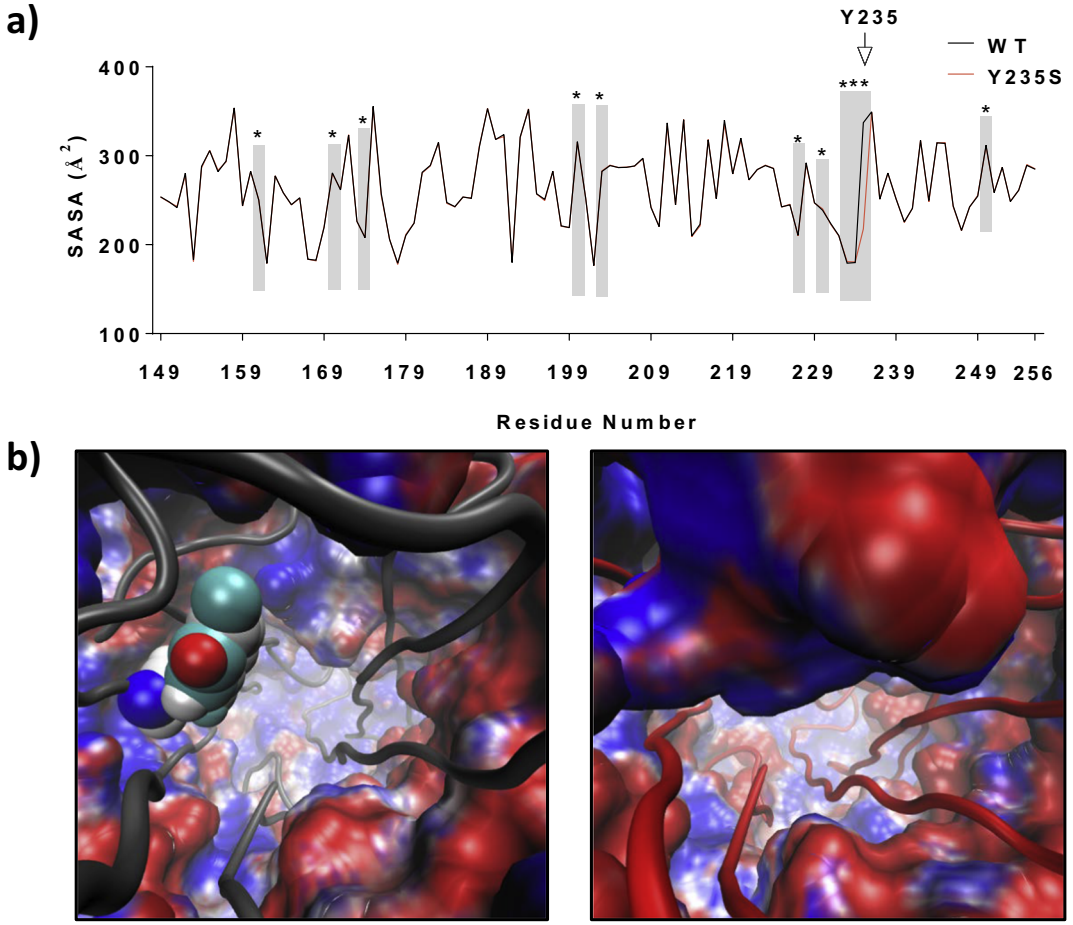

Fig. 9. C1 domain surface features and domain conformation **(a)** Averaged SASA per residues spanning D149 to E256 for the WT and Y235S C1 domains. MDS results showed that there were 11 residues with significant changes in SASA as a result of the Y235S mutation. Values are expressed as mean ± S.D.; * $P < 0.05$. **(b)** A volume slice image of WT (left) and Y235S (right). It shows the solvent accessible volume bulging into the hydrophobic core of the C1 domain. Residue 235 is shown in VDW. VMD was used to obtain data and render the image.

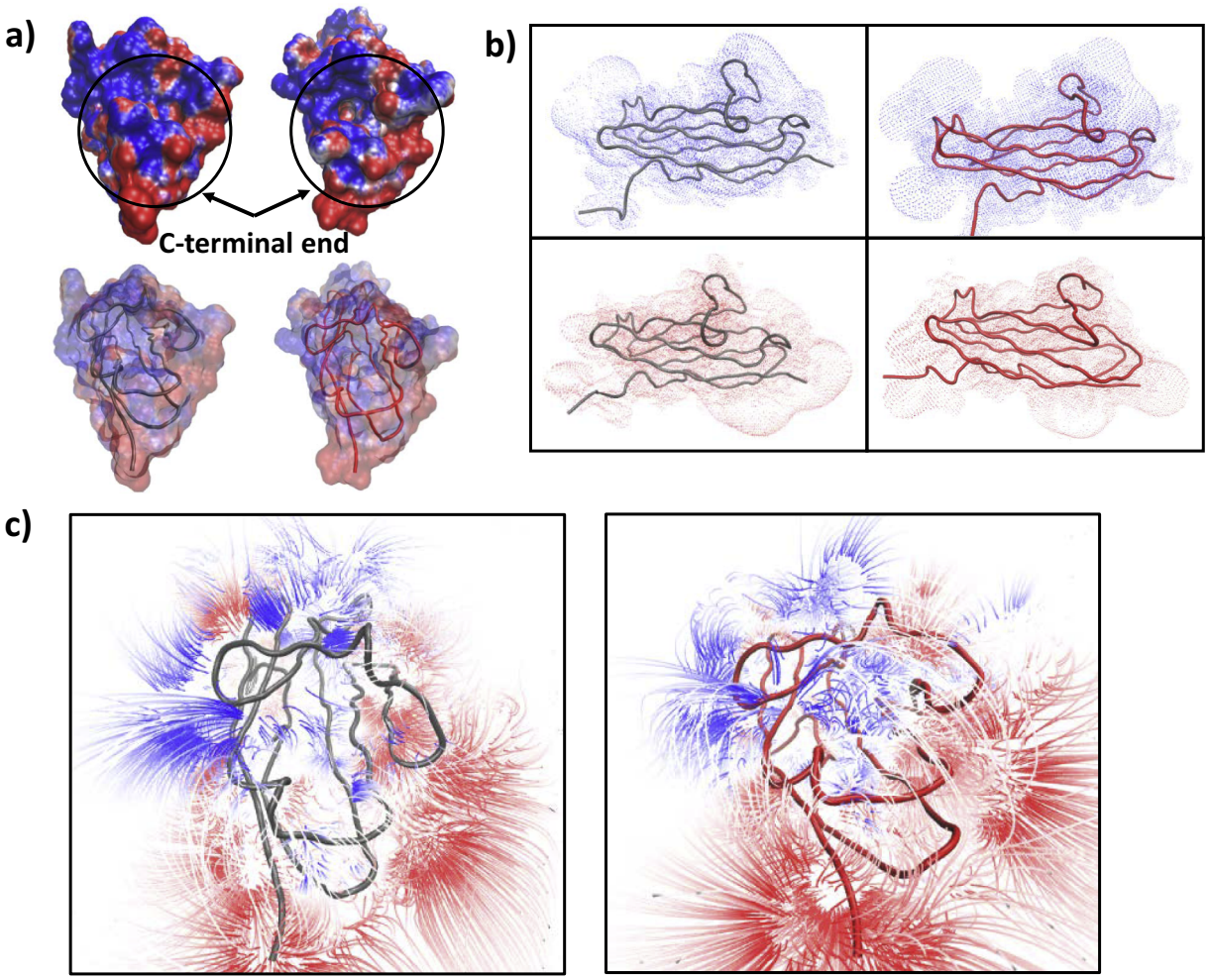

Fig. 10. Representative electrostatic potentials maps and potentials **(a)** Electrostatic potential mapped onto solvent accessible surface for WT (upper left) and Y235S mutant (upper right) C-terminal end of C1 domains. The corresponding cartoon representation of WT (gray) and Y235S (red) are shown in the lower images. **(b)** Positive (top) and negative (bottom) electrostatic isocontour images of WT and Y235S overlaid on SASA. N-terminal end of C1 domain is on the left side of each image. **(c)** A representative image of electric field lines of WT and Y235S C-terminal ends. Blue, white, and red represent positive, neutral, and negative charges, respectively. Backbone structure of WT (gray) and Y235S (red) are shown for the electric potential, isocontour and field lines. All three figures show that there are alterations of charge density and electric potential in the C-terminal end of the mutant Y235S model. VMD was used to render the images.

the N-terminal end of C1 domain. This moved the positively charged D196 residue away from the C-terminal end, as well as changed the surface conformation of the C-terminal end. Additionally, the side chain size difference of tyrosine and serine is significant, such that the Y235S mutation was observed to alter the C-terminal end surface conformation and create a large solvent accessible bulge inside of the C1 domain (Fig. 9(b)). Since these Y235S mutation-induced displacement and alterations in hydrophobic and ionic bonds affected important actin binding residues, we can speculate that it may have contributed to improper cMyBPC-actin binding. Since the Y235S mutation did not cause any changes in the simulation parameters for the positively-charged four amino acid loop (R213-K216, in mouse sequence) shown to interact with TM [34], it is uncertain whether the mutation alters cMyBPC's interaction with TM. In summary, it is plausible that the above changes in the mutant cMyBPC have a role in causing inability to sustain proper thin filament activation, which may lead to accelerated XB detachment and increased magnitude of XB detachment as reported in earlier studies [47,51].

A reduction in P1 (XB stiffness) in the mutant Y235S model was also noted. P1 is a measure of the intrinsic property of strongly bound XBs, and cannot be attributed to the number of strongly-bound XBs prior to inducing stretch because our experiments were force matched and normalized. The aberrant interaction between cMyBPC and actin may relieve the load that myosin is required to pull in order to proceed with a power stroke cycle. The observed decrease in P1 is similar to the effects of cMyBPC ablation [107] and PKA phosphorylation of cMyBPC [108]. Our data show that reduced P1 due to Y235S mutation is also accompanied by accelerated rate of XB detachment (k_{rel}). This finding is in good agreement with our previous reports which suggest that decreased XB stiffness may enhance XB compliance such that XBs detach rapidly following a sudden stretch in muscle length [51,109,110]. Conversely, there is data to show that increased XB stiffness, likely due to conformational changes of myosin heads upon binding of the myosin activator omecamtiv mecarbil, can prolong the duration of XBs in their actin-attached state and slow k_{rel} [49]. The only significant secondary structural change that is seen with the Y235S mutation that may contribute to aberrant intermolecular interactions, other than temporary fluctuations, are the conversion of residues T229-G233 and F250-L252 from an alpha helix and extended β-sheet conformation, respectively, to disorganized random coils (Fig. 8). However, along with the changes in cMyBPC electrostatic potentials near its actin binding region, it appears that the Y235S mutations may have contributed to reduced P1, which then accelerated k_{rel} as expected (Table 2).

Moreover, the expression of Y235S cMyBPC significantly enhanced Ca^{2+} sensitivity and reduced n_H suggesting that this mutation promoted cooperative XB activation and binding to the thin filaments at low Ca^{2+}

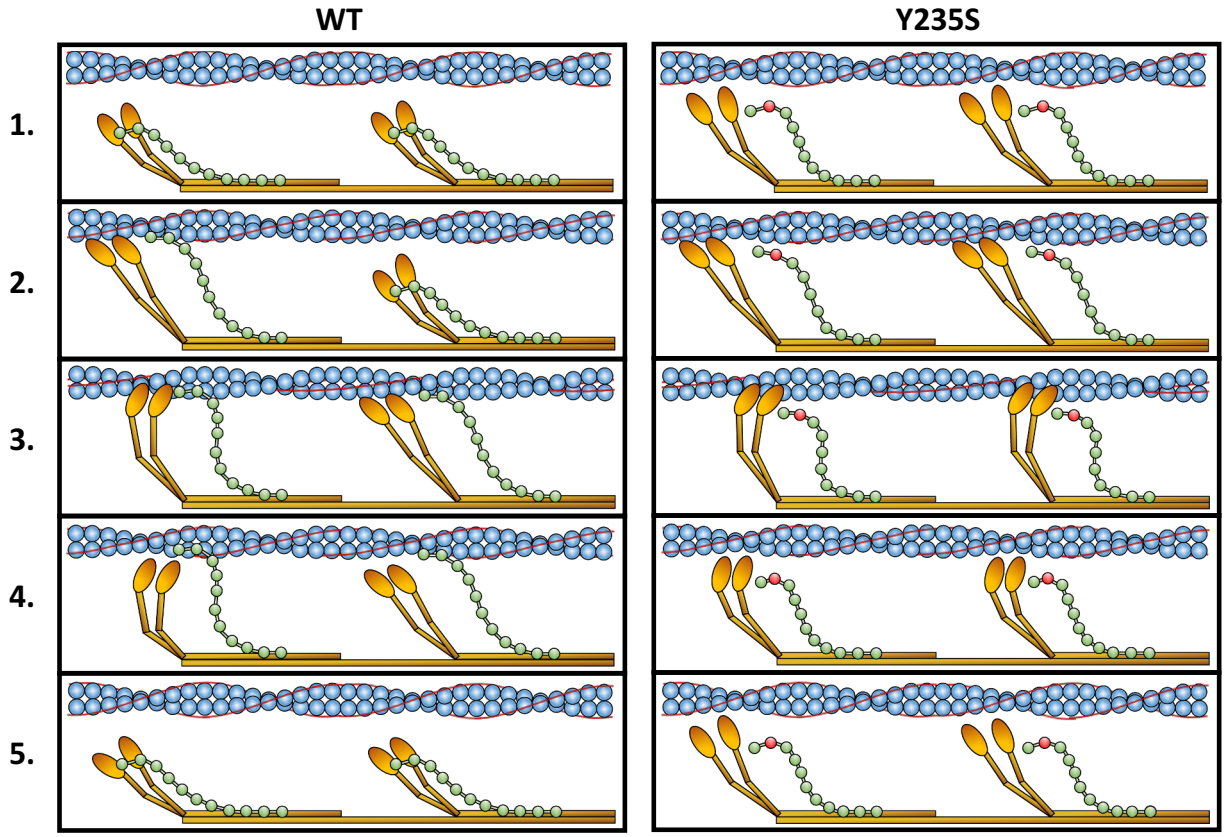

Fig. 11. Theoretical model of the altered XB kinetics due to the Y235S mutation. Left panels show the XB formation of the WT cMyBPC: 1) In the relaxation phase, cMyBPC inhibits XB formation by tethering to myosin S1 and/or S2. 2) Potentiation of the thin filament causes some myosin molecules to bind actin weakly. cMyBPC aids in the thin filament activation but the XB recruitment rate is kept at a low rate due to cMyBPC's initial inhibition of myosin. 3) At high levels of activation, cMyBPC interacts with actin to open myosin binding site on actin and myosin molecules undergo cycles of power strokes. However, the drag on the thin filament due to cMyBPC decreases shortening velocity, slows cycling rate and increases XB stiffness. 4) Myosin detaches from the thin filament, post power stroke. The detachment rate is decreased because cMyBPC is still attached to actin, keeping the myosin binding sites open. 5) The XBs return to the relaxation phase where myosin is inhibited by cMyBPC and actin filament is deactivated. Right panels show the corresponding phases of XB formation in the Y235S cMyBPC: 1) With the introduction of the Y235S mutation in the C1 domain of cMyBPC, proper interactions with myosin S1 and/or S2 may be ablated. Therefore, cMyBPC does not properly bind and inhibit myosin S1 and/or S2. Consequently, myosin molecules may be physically closer to actin, priming them for faster and greater magnitude of XB formation. 2) At low levels of Ca^{2+} activation, we see an increase in the rate of XB recruitment (k_{df}) of myosin in the mutant Y235S cMyBPC, because its inhibition on myosin is lifted. Although cMyBPC is also not able to properly interact with actin, we see an increase in pCa_{50} and decrease in n_H (increase in Ca^{2+} sensitivity) because Ca^{2+} and myosin are more potent activators of the thin filament. 3) At high Ca^{2+} levels, the lack of cMyBPC-actin interactions lead to increased force generation and accelerated cycling rate, increased shortening velocity, and decreased XB stiffness. 4) After the power stroke, cMyBPC is unable to keep myosin binding sites open for myosin to sustain the interaction with actin, contributing to an accelerated XB detachment (k_{rel}), as well as an increased magnitude of XB detachment. 5) The XBs unbind and return to their relaxed states. However, the myosin molecules are not properly inhibited by cMyBPC, so they are again primed for subsequent XB formation.

activations. This in turn increased steady-state force generation at forces < ~50% of maximal Ca^{2+} level (Fig. 4) by shifting the net equilibrium of myosin XBs towards the force-bearing states and enhancing the propagation of cooperative XB recruitment along the thin filament [111]. Previous studies have shown that N-terminal fragments of cMyBPC can displace TM under low Ca^{2+} conditions to cause actin filament interaction with myosin [112]. Thus, improper cMyBPC interaction with TM under low Ca^{2+} conditions due to mutations, may also cause improper actin activation. However, the enhanced XB recruitment at submaximal Ca^{2+} levels correspond to the prolonged late systolic ejection when Ca^{2+} levels have already declined. At the sarcomere level, Ca^{2+} and myosin are more potent activators of the thin filament where the magnitude of XB recruitment and binding to thin filaments is influenced by Ca^{2+} binding to cTnC followed by XB binding to actin [113]. Since the ejection phase of cardiac cycle is related to ventricular contraction and XB recruitment, changes in the Ca^{2+} sensitivity at the lower levels of Ca^{2+} primarily affect myosin XB function. Therefore, our results are compatible with the model where the effects of cMyBPC with actin dominates the XB "*on*" time following recruitment but may not be dominant in XB recruitment itself. In other words, as the level of Ca^{2+} activation increases, myofilament force generation becomes less reliant on cooperative XB recruitment because more thin filament regulatory units are directly activated by Ca^{2+}, such that the effect of Y235S cMyBPC on Ca^{2+} activated force generation is attenuated [22,51] (Fig. 4). In summary, our findings support the idea that cMyBPC interaction with actin may predominantly affect XB "*on*" time following recruitment, but the rate and magnitude of XB recruitment and Ca^{2+} sensitivity (leading to changes in the force-pCa curve) are likely due to cMyBPC's effect on myosin, rather than on actin.

In conclusion, we showed that the expression of Y235S cMyBPC disrupts the inter and intra molecular interactions of cMyBPC's C1 domain with myosin and actin using MDS, thereby accelerating recruitment of additional XBs to empty myosin binding sites on actin and XB transitions to force-bearing states [111,112,114]. Decreased binding to actin due to Y235S expression may lead to a corresponding accelerated XB detachment rate (k_{rel}) and reduced XB "*on*" time, which accelerates the overall XB turnover rate and shortening velocity [112]. The major results are summarized in a theoretical model of XB kinetics of the WT

and the Y235S mutation (Fig. 11). Since many protein-protein interactions depend on shape and charge complementarity, changes in the shape of the binding surface interface or electrostatic charge identified using MDS may also explain our in vitro experimental observations. In short, our results demonstrated that a single missense mutation in the C1 domain of cMyBPC alters the rate of XB cycling and overall contractile behavior of cardiac muscle by destabilizing key residues responsible for actomyosin interaction and disrupting actomyosin binding by altering intramolecular interactions, domain stability/structure, and surface electrostatic potentials. At the myofilament level, significant accelerations in XB recruitment and detachment rates results in enhanced ATP turnover rates, reducing the XB duty ratio. At the whole-heart level, a chronically elevated ATP turnover rate leads to myocardial energetic deficits that in part underlie HCM-mediated in vivo contractile dysfunction, hypertrophy [11], or diastolic dysfunction [115,116].

Transparency document

The Transparency document associated with this article can be found, in online version.

CRediT authorship contribution statement

Chang Yoon Doh: Conceptualization, Methodology, Validation, Formal analysis, Investigation, Data curation, Writing-original draft, Writing-review & editing, Visualization. **Jiayang Li:** Methodology, Validation, Formal analysis, Investigation, Resources, Data curation, Writing-review & editing, Funding acquisition. **Ranganath Mamidi:** Methodology, Validation, Formal analysis, Investigation, Resources, Data curation, Writing-review & editing, Funding acquisition. **Julian E. Stelzer:** Conceptualization, Methodology, Validation, Formal analysis, Investigation, Resources, Data curation, Writing-original draft, Writing-review & editing, Supervision, Project administration, Funding acquisition.

Acknowledgements

This work made use of the High Performance Computing Resource in the Core Facility for Advanced Research Computing at Case Western Reserve University for molecular dynamics simulations. This work was supported by the Theoretical and Computational Biophysics group, NIH Center for Macromolecular Modeling and Bioinformatics, at the Beckman Institute, University of Illinois at Urbana-Champaign.

Funding

This work was supported by the National Institutes of Health (HL-114770, T32-HL007567, and GM007250) and the American Heart Association (16POST30730000).

Accession numbers

The accession numbers reported in this paper includes C1 domain structure of cMyBPC (PDB: 2V6H, 3CX2, 2AVG, and 4EDQ).

Conflict of financial interests

The authors declare no competing financial interest.

References

[1] L. Carrier, G. Mearini, K. Stathopoulou, F. Cuello, Cardiac myosin-binding protein C (MYBPC3) in cardiac pathophysiology, Gene 573 (2015) 188–197, https://doi.org/10.1016/j.gene.2015.09.008.
[2] C. Semsarian, J. Ingles, M.S. Maron, B.J. Maron, New perspectives on the prevalence of hypertrophic cardiomyopathy, J. Am. Coll. Cardiol. 65 (2015) 1249–1254, https://doi.org/10.1016/j.jacc.2015.01.019.
[3] L.M. Baudhuin, K.E. Kotzer, M.L. Kluge, J.J. Maleszewski, What is the true prevalence of hypertrophic cardiomyopathy? J. Am. Coll. Cardiol. 66 (2015) 1845–1846, https://doi.org/10.1016/j.jacc.2015.07.074.
[4] B.J. Maron, M.S. Maron, Hypertrophic cardiomyopathy, Lancet 381 (2013) 242–255, https://doi.org/10.1016/S0140-6736(12)60397-3.
[5] Authors/Task Force members, P.M. Elliott, A. Anastasakis, M.A. Borger, M. Borggrefe, F. Cecchi, P. Charron, A.A. Hagege, A. Lafont, G. Limongelli, H. Mahrholdt, W.J. McKenna, J. Mogensen, P. Nihoyannopoulos, S. Nistri, P.G. Pieper, B. Pieske, C. Rapezzi, F.H. Rutten, C. Tillmanns, H. Watkins, 2014 ESC guidelines on diagnosis and management of hypertrophic cardiomyopathy: the task force for the diagnosis and management of hypertrophic cardiomyopathy of the European Society of Cardiology (ESC), Eur. Heart J. 35 (2014) 2733–2779, https://doi.org/10.1093/eurheartj/ehu284.
[6] B.J. Maron, J.M. Gardin, J.M. Flack, S.S. Gidding, T.T. Kurosaki, D.E. Bild, Prevalence of hypertrophic cardiomyopathy in a general population of young adults. Echocardiographic analysis of 4111 subjects in the CARDIA study. Coronary artery risk development in (young) adults, Circulation 92 (1995) 785–789 http://www.ncbi.nlm.nih.gov/pubmed/7641357.
[7] J. van der Velden, C.Y. Ho, J.C. Tardiff, I. Olivotto, B.C. Knollmann, L. Carrier, Research priorities in sarcomeric cardiomyopathies, Cardiovasc. Res. 105 (2015) 449–456, https://doi.org/10.1093/cvr/cvv019.
[8] C.Y. Ho, C. Carlsen, J.J. Thune, O. Havndrup, H. Bundgaard, F. Farrohi, J. Rivero, A.L. Cirino, P.S. Andersen, M. Christiansen, B.J. Maron, E.J. Orav, L. Køber, Echocardiographic strain imaging to assess early and late consequences of sarcomere mutations in hypertrophic cardiomyopathy, Circ. Cardiovasc. Genet. 2 (2009) 314–321, https://doi.org/10.1161/CIRCGENETICS.109.862128.
[9] C.Y. Ho, N.K. Sweitzer, B. McDonough, B.J. Maron, S.A. Casey, J.G. Seidman, C.E. Seidman, S.D. Solomon, Assessment of diastolic function with Doppler tissue imaging to predict genotype in preclinical hypertrophic cardiomyopathy, Circulation 105 (2002) 2992–2997, https://doi.org/10.1161/01.CIR.0000019070.70491.6D.
[10] J.A. Spudich, Hypertrophic and dilated cardiomyopathy: four decades of basic research on muscle lead to potential therapeutic approaches to these devastating genetic diseases, Biophys. J. 106 (2014) 1236–1249, https://doi.org/10.1016/j.bpj.2014.02.011.
[11] E.R. Witjas-Paalberends, C. Ferrara, B. Scellini, N. Piroddi, J. Montag, C. Tesi, G.J.M. Stienen, M. Michels, C.Y. Ho, T. Kraft, C. Poggesi, J. van der Velden, Faster cross-bridge detachment and increased tension cost in human hypertrophic cardiomyopathy with the R403Q MYH7 mutation, J. Physiol. 592 (2014) 3257–3272, https://doi.org/10.1113/jphysiol.2014.274571.
[12] J. Li, K.S. Gresham, R. Mamidi, C.Y. Doh, X. Wan, I. Deschenes, J.E. Stelzer, Sarcomere-based genetic enhancement of systolic cardiac function in a murine model of dilated cardiomyopathy, Int. J. Cardiol. 273 (2018) 168–176, https://doi.org/10.1016/j.ijcard.2018.09.073.
[13] X. Ren, N. Hensley, M.B. Brady, W.D. Gao, The genetic and molecular bases for hypertrophic cardiomyopathy: the role for calcium sensitization, J. Cardiothorac. Vasc. Anesth. 32 (2018) 478–487, https://doi.org/10.1053/j.jvca.2017.05.035.
[14] A.A. Alfares, M.A. Kelly, G. McDermott, B.H. Funke, M.S. Lebo, S.B. Baxter, J. Shen, H.M. McLaughlin, E.H. Clark, L.J. Babb, S.W. Cox, S.R. DePalma, C.Y. Ho, J.G. Seidman, C.E. Seidman, H.L. Rehm, Results of clinical genetic testing of 2,912 probands with hypertrophic cardiomyopathy: expanded panels offer limited additional sensitivity, Genet. Med. 17 (2015) 880–888, https://doi.org/10.1038/gim.2014.205.
[15] J. Gómez, J.R. Reguero, E. Coto, The ups and downs of genetic diagnosis of hypertrophic cardiomyopathy, Rev. Esp. Cardiol. (Engl. Ed) 69 (2016) 61–68, https://doi.org/10.1016/j.rec.2015.10.001.
[16] W. Liu, W. Liu, D. Hu, T. Zhu, Z. Ma, J. Yang, W. Xie, C. Li, L. Li, J. Yang, T. Li, H. Bian, Q. Tong, Mutation spectrum in a large cohort of unrelated Chinese patients with hypertrophic cardiomyopathy, Am. J. Cardiol. 112 (2013) 585–589, https://doi.org/10.1016/j.amjcard.2013.04.021.
[17] S.P. Harris, R.G. Lyons, K.L. Bezold, In the thick of it, Circ. Res. 108 (2011) 751–764 http://circres.ahajournals.org/content/108/6/751.abstract.
[18] H. Morita, H.L. Rehm, A. Menesses, B. McDonough, A.E. Roberts, R. Kucherlapati, J.A. Towbin, J.G. Seidman, C.E. Seidman, Shared genetic causes of cardiac hypertrophy in children and adults, N. Engl. J. Med. 358 (2008) 1899–1908, https://doi.org/10.1056/NEJMoa075463.
[19] L. Carrier, G. Mearini, K. Stathopoulou, F. Cuello, Cardiac myosin-binding protein C (MYBPC3) in cardiac pathophysiology, Gene 573 (2015) 188–197, https://doi.org/10.1016/j.gene.2015.09.008.
[20] J.F. Shaffer, R.W. Kensler, S.P. Harris, The myosin-binding protein C motif binds to F-actin in a phosphorylation-sensitive manner, J. Biol. Chem. 284 (2009) 12318–12327, https://doi.org/10.1074/jbc.M808850200.
[21] T. Kampourakis, Z. Yan, M. Gautel, Y.-B. Sun, M. Irving, Myosin binding protein-C activates thin filaments and inhibits thick filaments in heart muscle cells, Proc. Natl. Acad. Sci. U. S. A. 111 (2014) 18763–18768, https://doi.org/10.1073/pnas.1413922112.
[22] M.J. Previs, J.Y. Mun, A.J. Michalek, S.B. Previs, J. Gulick, J. Robbins, D.M. Warshaw, R. Craig, Phosphorylation and calcium antagonistically tune myosin-binding protein C's structure and function, Proc. Natl. Acad. Sci. U. S. A. 113 (2016) 3239–3244, https://doi.org/10.1073/pnas.1522236113.
[23] S. Nag, D.V. Trivedi, S.S. Sarkar, A.S. Adhikari, M.S. Sunitha, S. Sutton, K.M. Ruppel, J.A. Spudich, The myosin mesa and the basis of hypercontractility caused by hypertrophic cardiomyopathy mutations, Nat. Struct. Mol. Biol. (2017), https://doi.org/10.1038/nsmb.3408.

[24] D.V. Trivedi, A.S. Adhikari, S.S. Sarkar, K.M. Ruppel, J.A. Spudich, Hypertrophic cardiomyopathy and the myosin mesa: viewing an old disease in a new light, Biophys. Rev. (2018), https://doi.org/10.1007/s12551-017-0274-6.
[25] R. Craig, K.H. Lee, J.Y. Mun, I. Torre, P.K. Luther, Structure, sarcomeric organization, and thin filament binding of cardiac myosin-binding protein-C, Pflugers Arch. 466 (2014) 425–431, https://doi.org/10.1007/s00424-013-1426-6.
[26] M.J. Previs, A.J. Michalek, D.M. Warshaw, Molecular modulation of actomyosin function by cardiac myosin-binding protein C, Pflugers Arch. 466 (2014) 439–444, https://doi.org/10.1007/s00424-013-1433-7.
[27] J. Moolman-Smook, E. Flashman, W. de Lange, Z. Li, V. Corfield, C. Redwood, H. Watkins, Identification of novel interactions between domains of myosin binding protein-C that are modulated by hypertrophic cardiomyopathy missense mutations, Circ. Res. 91 (2002) 704–711 https://doi.org/10.1161/01.RES.0000036750.81083.83.
[28] E. Flashman, L. Korkie, H. Watkins, C. Redwood, J.C. Moolman-Smook, Support for a trimeric collar of myosin binding protein C in cardiac and fast skeletal muscle, but not in slow skeletal muscle, FEBS Lett. 582 (2008) 434–438, https://doi.org/10.1016/j.febslet.2008.01.004.
[29] R. Gilbert, M.G. Kelly, T. Mikawa, D.A. Fischman, The carboxyl terminus of myosin binding protein C (MyBP-C, C-protein) specifies incorporation into the A-band of striated muscle, J. Cell Sci. 109 (1) (1996) 101–111 http://www.ncbi.nlm.nih.gov/pubmed/8834795.
[30] S.P. Harris, B. Belknap, R.E. Van Sciver, H.D. White, V.E. Galkin, C0 and C1 N-terminal Ig domains of myosin binding protein C exert different effects on thin filament activation, Proc. Natl. Acad. Sci. U. S. A. 113 (2016), https://doi.org/10.1073/pnas.1518891113.
[31] A. Ababou, E. Rostkova, S. Mistry, C. Le Masurier, M. Gautel, M. Pfuhl, Myosin binding protein C positioned to play a key role in regulation of muscle contraction: structure and interactions of domain C1, J. Mol. Biol. (2008), https://doi.org/10.1016/j.jmb.2008.09.065.
[32] Y. Lu, A.H. Kwan, J. Trewhella, C.M. Jeffries, The C0C1 fragment of human cardiac myosin binding protein C has common binding determinants for both actin and myosin, J. Mol. Biol. 413 (2011) 908–913, https://doi.org/10.1016/j.jmb.2011.09.026.
[33] M.S. Bhuiyan, J. Gulick, H. Osinska, M. Gupta, J. Robbins, Determination of the critical residues responsible for cardiac myosin binding protein C's interactions, J. Mol. Cell. Cardiol. 53 (2012) 838–847, https://doi.org/10.1016/j.yjmcc.2012.08.028.
[34] C. Risi, B. Belknap, E. Forgacs-Lonart, S.P. Harris, G.F. Schröder, H.D. White, V.E. Galkin, N-terminal domains of cardiac myosin binding protein C cooperatively activate the thin filament, Structure (2018) 1–8, https://doi.org/10.1016/j.str.2018.08.007.
[35] S.P. Harris, R.G. Lyons, K.L. Bezold, In the thick of it: HCM-causing mutations in myosin binding proteins of the thick filament, Circ. Res. 108 (2011) 751–764, https://doi.org/10.1161/CIRCRESAHA.110.231670.
[36] S. Mörner, P. Richard, E. Kazzam, U. Hellman, B. Hainque, K. Schwartz, A. Waldenström, Identification of the genotypes causing hypertrophic cardiomyopathy in northern Sweden, J. Mol. Cell. Cardiol. 35 (2003) 841–849, https://doi.org/10.1016/S0022-2828(03)00146-9.
[37] M. García-Castro, E. Coto, J.R. Reguero, J.R. Berrazueta, V. Alvarez, B. Alonso, R. Sainz, M. Martín, C. Morís, Mutations in sarcomeric genes MYH7, MYBPC3, TNNT2, TNNI3, and TPM1 in patients with hypertrophic cardiomyopathy, Rev. Esp. Cardiol. 62 (2009) 48–56, https://doi.org/10.1016/S1885-5857(09)71513-0.
[38] L. Govada, L. Carpenter, P.C.A. da Fonseca, J.R. Helliwell, P. Rizkallah, E. Flashman, N.E. Chayen, C. Redwood, J.M. Squire, Crystal structure of the C1 domain of cardiac myosin binding protein-C: implications for hypertrophic cardiomyopathy, J. Mol. Biol. 378 (2008) 387–397, https://doi.org/10.1016/j.jmb.2008.02.044.
[39] C.E. Oakley, B.D. Hambly, P.M.G. Curmi, L.J. Brown, Myosin binding protein C: structural abnormalities in familial hypertrophic cardiomyopathy, Cell Res. 14 (2004) 95–110, https://doi.org/10.1038/sj.cr.7290208.
[40] S. Merkulov, X. Chen, M.P. Chandler, J.E. Stelzer, In vivo cardiac myosin binding protein C gene transfer rescues myofilament contractile dysfunction in cardiac myosin binding protein C null mice, Circ. Heart Fail. 5 (2012) 635–644, https://doi.org/10.1161/CIRCHEARTFAILURE.112.968941.
[41] K.S. Gresham, R. Mamidi, J.E. Stelzer, The contribution of cardiac myosin binding protein-c Ser282 phosphorylation to the rate of force generation and in vivo cardiac contractility, J. Physiol. 592 (2014) 3747–3765, https://doi.org/10.1113/jphysiol.2014.276022.
[42] C.A. Schneider, W.S. Rasband, K.W. Eliceiri, NIH image to ImageJ: 25 years of image analysis, Nat. Methods 9 (2012) 671–675, https://doi.org/10.1038/nmeth.2089.
[43] K.S. Gresham, R. Mamidi, J. Li, H. Kwak, J.E. Stelzer, Sarcomeric protein modification during adrenergic stress enhances cross-bridge kinetics and cardiac output, J. Appl. Physiol. 122 (2017) 520–530, https://doi.org/10.1152/japplphysiol.00306.2016.
[44] A. Fabiato, Computer programs for calculating total from specified free or free from specified total ionic concentrations in aqueous solutions containing multiple metals and ligands, Methods Enzymol. 157 (1988) 378–417 http://www.ncbi.nlm.nih.gov/pubmed/3231093.
[45] R.E. Godt, B.D. Lindley, Influence of temperature upon contractile activation and isometric force production in mechanically skinned muscle fibers of the frog, J. Gen. Physiol. 80 (1982) 279–297, https://doi.org/10.1085/jgp.80.2.279.
[46] R. Mamidi, J. Li, K.S. Gresham, S. Verma, C.Y. Doh, A. Li, S. Lal, C.G. Dos Remedios, J.E. Stelzer, Dose-dependent effects of the myosin activator Omecamtiv Mecarbil on cross-bridge behavior and force generation in failing human myocardium, Circ. Heart Fail. 10 (2017), https://doi.org/10.1161/CIRCHEARTFAILURE.117.004257.
[47] R. Mamidi, K.S. Gresham, J. Li, J.E. Stelzer, Cardiac myosin binding protein-C Ser (302) phosphorylation regulates cardiac β-adrenergic reserve, Sci. Adv. (3) (2017) e1602445, , https://doi.org/10.1126/sciadv.1602445.
[48] K.S. Campbell, R.L. Moss, SLControl: PC-based data acquisition and analysis for muscle mechanics, Am. J. Physiol. Heart Circ. Physiol. 285 (2003) H2857–H2864, https://doi.org/10.1152/ajpheart.00295.2003.
[49] R. Mamidi, K.S. Gresham, A. Li, C.G. dos Remedios, J.E. Stelzer, Molecular effects of the myosin activator omecamtiv mecarbil on contractile properties of skinned myocardium lacking cardiac myosin binding protein-C, J. Mol. Cell. Cardiol. 85 (2015) 262–272, https://doi.org/10.1016/j.yjmcc.2015.06.011.
[50] R. Mamidi, J. Li, C.Y. Doh, S. Verma, J.E. Stelzer, Impact of the Myosin Modulator Mavacamten on Force Generation and Cross-Bridge Behavior in a Murine Model of Hypercontractility, J. Am. Heart Assoc. 7 (2018) 1–15, https://doi.org/10.1161/JAHA.118.009627.
[51] R. Mamidi, K.S. Gresham, S. Verma, J.E. Stelzer, Cardiac myosin binding protein-C phosphorylation modulates myofilament length-dependent activation, Front. Physiol. 7 (2016) 38, , https://doi.org/10.3389/fphys.2016.00038.
[52] S.J. Ford, M. Chandra, R. Mamidi, W. Dong, K.B. Campbell, Model representation of the nonlinear step response in cardiac muscle, J. Gen. Physiol. 136 (2010) 159–177, https://doi.org/10.1085/jgp.201010467.
[53] W. Li, A. Cowley, M. Uludag, T. Gur, H. McWilliam, S. Squizzato, Y.M. Park, N. Buso, R. Lopez, The EMBL-EBI bioinformatics web and programmatic tools framework, Nucleic Acids Res. 43 (2015) W580–W584, https://doi.org/10.1093/nar/gkv279.
[54] H. McWilliam, W. Li, M. Uludag, S. Squizzato, Y.M. Park, N. Buso, A.P. Cowley, R. Lopez, Analysis tool web services from the EMBL-EBI, Nucleic Acids Res. 41 (2013) W597–W600, https://doi.org/10.1093/nar/gkt376.
[55] F. Sievers, A. Wilm, D. Dineen, T.J. Gibson, K. Karplus, W. Li, R. Lopez, H. McWilliam, M. Remmert, J. Söding, J.D. Thompson, D.G. Higgins, Fast, scalable generation of high-quality protein multiple sequence alignments using Clustal omega, Mol. Syst. Biol. 7 (2011) 539, https://doi.org/10.1038/msb.2011.75.
[56] N.P. Brown, C. Leroy, C. Sander, MView: a web-compatible database search or multiple alignment viewer, Bioinformatics 14 (1998) 380–381, https://doi.org/10.1093/bioinformatics/14.4.380.
[57] W.R. Taylor, Identification of protein sequence homology by consensus template alignment, J. Mol. Biol. 188 (1986) 233–258, https://doi.org/10.1016/0022-2836(86)90308-6.
[58] M. Wiederstein, M.J. Sippl, ProSA-web: interactive web service for the recognition of errors in three-dimensional structures of proteins, Nucleic Acids Res. (2007), https://doi.org/10.1093/nar/gkm290.
[59] J.U. Bowie, R. Lüthy, D. Eisenberg, A method to identify protein sequences that fold into a known three-dimensional stucture, Science (1991), https://doi.org/10.1126/science.1853201 (80-.).
[60] R. Lüthy, J.U. Bowie, D. Eisenberg, Assessment of protein models with three-dimensional profiles, Nature (1992), https://doi.org/10.1038/356083a0.
[61] S. Jo, T. Kim, V.G. Iyer, W. Im, CHARMM-GUI: a web-based graphical user interface for CHARMM, J. Comput. Chem. 29 (2008) 1859–1865, https://doi.org/10.1002/jcc.20945.
[62] J. Lee, X. Cheng, J.M. Swails, M.S. Yeom, P.K. Eastman, J.A. Lemkul, S. Wei, J. Buckner, J.C. Jeong, Y. Qi, S. Jo, V.S. Pande, D.A. Case, C.L. Brooks, A.D. MacKerell, J.B. Klauda, W. Im, CHARMM-GUI input generator for NAMD, GROMACS, AMBER, OpenMM, and CHARMM/OpenMM simulations using the CHARMM36 additive force field, J. Chem. Theory Comput. 12 (2016) 405–413, https://doi.org/10.1021/acs.jctc.5b00935.
[63] V. Parthiban, M.M. Gromiha, D. Schomburg, CUPSAT: prediction of protein stability upon point mutations, Nucleic Acids Res. 34 (2006) W239–W242, https://doi.org/10.1093/nar/gkl190.
[64] J. Schymkowitz, J. Borg, F. Stricher, R. Nys, F. Rousseau, L. Serrano, The FoldX web server: an online force field, Nucleic Acids Res. 33 (2005) W382–W388, https://doi.org/10.1093/nar/gki387.
[65] S. Yin, F. Ding, N.V. Dokholyan, Eris: an automated estimator of protein stability, Nat. Methods 4 (2007) 466–467, https://doi.org/10.1038/nmeth0607-466.
[66] Y. Dehouck, J.M. Kwasigroch, D. Gilis, M. Rooman, PoPMuSiC 2.1: a web server for the estimation of protein stability changes upon mutation and sequence optimality, BMC Bioinf. 12 (2011) 151, https://doi.org/10.1186/1471-2105-12-151.
[67] L. Quan, Q. Lv, Y. Zhang, STRUM: structure-based prediction of protein stability changes upon single-point mutation, Bioinformatics 32 (2016) 2936–2946, https://doi.org/10.1093/bioinformatics/btw361.
[68] A.P. Pandurangan, B. Ochoa-Montaño, D.B. Ascher, T.L. Blundell, SDM: a server for predicting effects of mutations on protein stability, Nucleic Acids Res. 45 (2017) W229–W235, https://doi.org/10.1093/nar/gkx439.
[69] D.E.V. Pires, D.B. Ascher, T.L. Blundell, DUET: a server for predicting effects of mutations on protein stability using an integrated computational approach, Nucleic Acids Res. 42 (2014) W314–W319, https://doi.org/10.1093/nar/gku411.
[70] C.H.M. Rodrigues, D.E.V. Pires, D.B. Ascher, DynaMut: predicting the impact of mutations on protein conformation, flexibility and stability, Nucleic Acids Res. 46 (2018) W350–W355, https://doi.org/10.1093/nar/gky300.
[71] D.E.V. Pires, D.B. Ascher, T.L. Blundell, mCSM: predicting the effects of mutations in proteins using graph-based signatures, Bioinformatics 30 (2014) 335–342, https://doi.org/10.1093/bioinformatics/btt691.
[72] M. Masso, I.I. Vaisman, AUTO-MUTE: web-based tools for predicting stability changes in proteins due to single amino acid replacements, Protein Eng. Des. Sel. 23 (2010) 683–687, https://doi.org/10.1093/protein/gzq042.
[73] E. Capriotti, P. Fariselli, R. Casadio, I-Mutant2.0: predicting stability changes upon

mutation from the protein sequence or structure, Nucleic Acids Res. 33 (2005) W306–W310, https://doi.org/10.1093/nar/gki375.
[74] J. Cheng, A. Randall, P. Baldi, Prediction of protein stability changes for single-site mutations using support vector machines, Proteins Struct. Funct. Genet. 62 (2006) 1125–1132, https://doi.org/10.1002/prot.20810.
[75] V. Frappier, M. Chartier, R.J. Najmanovich, ENCoM server: exploring protein conformational space and the effect of mutations on protein function and stability, Nucleic Acids Res. 43 (2015) W395–W400, https://doi.org/10.1093/nar/gkv343.
[76] L.T. Huang, M.M. Gromiha, S.Y. Ho, iPTREE-STAB: interpretable decision tree based method for predicting protein stability changes upon mutations, Bioinformatics (2007), https://doi.org/10.1093/bioinformatics/btm100.
[77] F. Pucci, R. Bourgeas, M. Rooman, Predicting protein thermal stability changes upon point mutations using statistical potentials: introducing HoTMuSiC, Sci. Rep. 6 (2016) 23257, , https://doi.org/10.1038/srep23257.
[78] I.W. Davis, A. Leaver-Fay, V.B. Chen, J.N. Block, G.J. Kapral, X. Wang, L.W. Murray, W.B. Arendall, J. Snoeyink, J.S. Richardson, D.C. Richardson, MolProbity: all-atom contacts and structure validation for proteins and nucleic acids, Nucleic Acids Res. (2007), https://doi.org/10.1093/nar/gkm216.
[79] V.B. Chen, W.B. Arendall, J.J. Headd, D.A. Keedy, R.M. Immormino, G.J. Kapral, L.W. Murray, J.S. Richardson, D.C. Richardson, MolProbity: all-atom structure validation for macromolecular crystallography, Acta Crystallogr. Sect. D: Biol. Crystallogr. (2010), https://doi.org/10.1107/S0907444909042073.
[80] J.C. Phillips, R. Braun, W. Wang, J. Gumbart, E. Tajkhorshid, E. Villa, C. Chipot, R.D. Skeel, L. Kalé, K. Schulten, Scalable molecular dynamics with NAMD, J. Comput. Chem. 26 (2005) 1781–1802, https://doi.org/10.1002/jcc.20289.
[81] B.R. Brooks, C.L. Brooks, A.D. Mackerell, L. Nilsson, R.J. Petrella, B. Roux, Y. Won, G. Archontis, C. Bartels, S. Boresch, A. Caflisch, L. Caves, Q. Cui, A.R. Dinner, M. Feig, S. Fischer, J. Gao, M. Hodoscek, W. Im, K. Kuczera, T. Lazaridis, J. Ma, V. Ovchinnikov, E. Paci, R.W. Pastor, C.B. Post, J.Z. Pu, M. Schaefer, B. Tidor, R.M. Venable, H.L. Woodcock, X. Wu, W. Yang, D.M. York, M. Karplus, CHARMM: the biomolecular simulation program, J. Comput. Chem. 30 (2009) 1545–1614, https://doi.org/10.1002/jcc.21287.
[82] A. Varshney, F.P. Brooks, W.V. Wright, Linearly scalable computation of smooth molecular surfaces, IEEE Comput. Graph. Appl. 14 (1994) 19–25, https://doi.org/10.1109/38.310720.
[83] W. Humphrey, A. Dalke, K. Schulten, VMD: visual molecular dynamics, J. Mol. Graph. 14 (1996) 33–38 27–8 https://doi.org/10.1016/0263-7855(96)00018-5.
[84] D. Frishman, P. Argos, Knowledge-based protein secondary structure assignment, Proteins 23 (1995) 566–579, https://doi.org/10.1002/prot.340230412.
[85] T.J. Dolinsky, J.E. Nielsen, J.A. McCammon, N.A. Baker, PDB2PQR: an automated pipeline for the setup of Poisson-Boltzmann electrostatics calculations, Nucleic Acids Res. 32 (2004) W665–W667, https://doi.org/10.1093/nar/gkh381.
[86] N.A. Baker, D. Sept, S. Joseph, M.J. Holst, J.A. McCammon, Electrostatics of nanosystems: application to microtubules and the ribosome, Proc. Natl. Acad. Sci. U. S. A. 98 (2001) 10037–10041, https://doi.org/10.1073/pnas.181342398.
[87] D. Piovesan, G. Minervini, S.C.E. Tosatto, The RING 2.0 web server for high quality residue interaction networks, Nucleic Acids Res. (2016), https://doi.org/10.1093/nar/gkw315.
[88] R. Mamidi, J. Li, C.Y. Doh, J.B. Holmes, J.E. Stelzer, Lost in translation: interpreting cardiac muscle mechanics data in clinical practice, Arch. Biochem. Biophys. (2018), https://doi.org/10.1016/j.abb.2018.12.021.
[89] S.J. Fisher, J.R. Helliwell, S. Khurshid, L. Govada, C. Redwood, J.M. Squire, N.E. Chayen, An investigation into the protonation states of the C1 domain of cardiac myosin-binding protein C, Acta Crystallogr. D Biol. Crystallogr. 64 (2008) 658–664, https://doi.org/10.1107/S0907444908008792.
[90] Y. Zhang, I-TASSER server for protein 3D structure prediction, BMC Bioinf. 9 (2008) 40, https://doi.org/10.1186/1471-2105-9-40.
[91] J. Yang, R. Yan, A. Roy, D. Xu, J. Poisson, Y. Zhang, The I-TASSER suite: protein structure and function prediction, Nat. Methods 12 (2015) 7–8, https://doi.org/10.1038/nmeth.3213.
[92] Y. Zhang, J. Skolnick, Scoring function for automated assessment of protein structure template quality, Proteins Struct. Funct. Genet. (2004), https://doi.org/10.1002/prot.20264.
[93] W. Blankenfeldt, N.H. Thomä, J.S. Wray, M. Gautel, I. Schlichting, Crystal structures of human cardiac beta-myosin II S2-Delta provide insight into the functional role of the S2 subfragment, Proc. Natl. Acad. Sci. U. S. A. 103 (2006) 17713–17717, https://doi.org/10.1073/pnas.0606741103.
[94] I.N. Rybakova, M.L. Greaser, R.L. Moss, Myosin binding protein C interaction with actin: characterization and mapping of the binding site, J. Biol. Chem. 286 (2011) 2008–2016, https://doi.org/10.1074/jbc.M110.170605.
[95] J.Y. Mun, J. Gulick, J. Robbins, J. Woodhead, W. Lehman, R. Craig, Electron microscopy and 3D reconstruction of F-actin decorated with cardiac myosin-binding protein C (cMyBP-C), J. Mol. Biol. 410 (2011) 214–225, https://doi.org/10.1016/j.jmb.2011.05.010.
[96] P.S. Andersen, O. Havndrup, H. Bundgaard, L.A. Larsen, J. Vuust, A.K. Pedersen, K. Kjeldsen, M. Christiansen, Genetic and phenotypic characterization of mutations in myosin-binding protein C (MYBPC3) in 81 families with familial hypertrophic cardiomyopathy: Total or partial haploinsufficiency, Eur. J. Hum. Genet. 12 (2004) 673–677, https://doi.org/10.1038/sj.ejhg.5201190.
[97] X. Liu, T. Jiang, C. Piao, X. Li, J. Guo, S. Zheng, X. Zhang, T. Cai, J. Du, Screening mutations of MYBPC3 in 114 unrelated patients with hypertrophic cardiomyopathy by targeted capture and next-generation sequencing, Sci. Rep. 5 (2015) 1–8, https://doi.org/10.1038/srep11411.
[98] A.S. Helms, F.M. Davis, D. Coleman, S.N. Bartolone, A.A. Glazier, F. Pagani, J.M. Yob, S. Sadayappan, E. Pedersen, R. Lyons, M.V. Westfall, R. Jones, M.W. Russell, S.M. Day, Sarcomere mutation-specific expression patterns in human hypertrophic cardiomyopathy, Circ. Cardiovasc. Genet. (2014), https://doi.org/10.1161/CIRCGENETICS.113.000448.
[99] S. Marston, O. Copeland, A. Jacques, K. Livesey, V. Tsang, W.J. McKenna, S. Jalilzadeh, S. Carballo, C. Redwood, H. Watkins, Evidence from human myectomy samples that MYBPC3 mutations cause hypertrophic cardiomyopathy through haploinsufficiency, Circ. Res. (2009), https://doi.org/10.1161/CIRCRESAHA.109.202440.
[100] L. Carrier, S. Schlossarek, M.S. Willis, T. Eschenhagen, The ubiquitin-proteasome system and nonsense-mediated mRNA decay in hypertrophic cardiomyopathy, Cardiovasc. Res. (2010), https://doi.org/10.1093/cvr/cvp247.
[101] S.J. Van Dijk, D. Dooijes, C. Dos Remedios, M. Michels, J.M.J. Lamers, S. Winegrad, S. Schlossarek, L. Carrier, F.J.T. Cate, G.J.M. Stienen, J. Der Van Velden, Cardiac myosin-binding protein C mutations and hypertrophic cardiomyopathy haploinsufficiency, deranged phosphorylation, and cardiomyocyte dysfunction, Circulation (2009), https://doi.org/10.1161/CIRCULATIONAHA.108.838672.
[102] D.F. Smelter, W.J. de Lange, W. Cai, Y. Ge, J.C. Ralphe, The HCM-linked W792R mutation in cardiac myosin-binding protein C reduces C6 FnIII domain stability, Am. J. Physiol. Heart Circ. Physiol. 314 (2018) H1179–H1191, https://doi.org/10.1152/ajpheart.00686.2017.
[103] W.J. De Lange, A.C. Grimes, L.F. Hegge, A.M. Spring, T.M. Brost, J.C. Ralphe, E258K HCM-causing mutation in cardiac MyBP-C reduces contractile force and accelerates twitch kinetics by disrupting the cMyBP-C and myosin S2 interaction, J. Gen. Physiol. 142 (2013) 241–255, https://doi.org/10.1085/jgp.201311018.
[104] L.G. Randles, I. Lappalainen, S.B. Fowler, B. Moore, S.J. Hamill, J. Clarke, Using model proteins to quantify the effects of pathogenic mutations in Ig-like proteins, J. Biol. Chem. 281 (2006) 24216–24226, https://doi.org/10.1074/jbc.M603593200.
[105] N. Tokuriki, D.S. Tawfik, Protein dynamism and evolvability, Science 324 (2009) 203–207, https://doi.org/10.1126/science.1169375.
[106] M. Gruen, M. Gautel, Mutations in [beta]-myosin S2 that cause familial hypertrophic cardiomyopathy (FHC) abolish the interaction with the regulatory domain of myosin-binding protein-C, J. Mol. Biol. 286 (1999) 933–949, https://doi.org/10.1006/jmbi.1998.2522.
[107] B.M. Palmer, D. Georgakopoulos, P.M. Janssen, Y. Wang, N.R. Alpert, D.F. Belardi, S.P. Harris, R.L. Moss, P.G. Burgon, C.E. Seidman, J.G. Seidman, D.W. Maughan, D.A. Kass, Role of cardiac myosin binding protein C in sustaining left ventricular systolic stiffening, Circ. Res. 94 (2004) 1249–1255, https://doi.org/10.1161/01.RES.0000126898.95550.31.
[108] J.E. Stelzer, J.R. Patel, R.L. Moss, Protein kinase A-mediated acceleration of the stretch activation response in murine skinned myocardium is eliminated by ablation of cMyBP-C, Circ. Res. 99 (2006) 884–890, https://doi.org/10.1161/01.RES.0000245191.34690.66.
[109] J.E. Stelzer, L. Larsson, D.P. Fitzsimons, R.L. Moss, Activation dependence of stretch activation in mouse skinned myocardium: implications for ventricular function, J. Gen. Physiol. 127 (2006) 95–107, https://doi.org/10.1085/jgp.200509432.
[110] Y. Cheng, X. Wan, T.A. McElfresh, X. Chen, K.S. Gresham, D.S. Rosenbaum, M.P. Chandler, J.E. Stelzer, Impaired contractile function due to decreased cardiac myosin binding protein C content in the sarcomere, Am. J. Physiol. Heart Circ. Physiol. 305 (2013) H52–H65, https://doi.org/10.1152/ajpheart.00929.2012.
[111] R.L. Moss, D.P. Fitzsimons, J.C. Ralphe, Cardiac MyBP-C regulates the rate and force of contraction in mammalian myocardium, Circ. Res. 116 (2015) 183–192, https://doi.org/10.1161/CIRCRESAHA.116.300561.
[112] J.Y. Mun, M.J. Previs, H.Y. Yu, J. Gulick, L.S. Tobacman, S. Beck Previs, J. Robbins, D.M. Warshaw, R. Craig, Myosin-binding protein C displaces tropomyosin to activate cardiac thin filaments and governs their speed by an independent mechanism, Proc. Natl. Acad. Sci. (2014), https://doi.org/10.1073/pnas.1316001111.
[113] A.M. Gordon, E. Homsher, M. Regnier, Regulation of contraction in striated muscle, Physiol. Rev. (2000), https://doi.org/10.1152/physrev.2000.80.2.853.
[114] B.A. Colson, J.R. Patel, P.P. Chen, T. Bekyarova, M.I. Abdalla, C.W. Tong, D.P. Fitzsimons, T.C. Irving, R.L. Moss, Myosin binding protein-C phosphorylation is the principal mediator of protein kinase A effects on thick filament structure in myocardium, J. Mol. Cell. Cardiol. (2012), https://doi.org/10.1016/j.yjmcc.2012.07.012.
[115] S. Dass, J. Suttie, T. Karamitsos, H. Watkins, S. Neubauer, Acute derangement of cardiac energy metabolism and oxygenation during stress in hypertrophic cardiomyopathy-a potential mechanism for sudden cardiac death, Heart (2012), https://doi.org/10.1136/heartjnl-2012-301877b.81.
[116] S. Dass, L.E. Cochlin, J.J. Suttie, C.J. Holloway, O.J. Rider, L. Carden, D.J. Tyler, T.D. Karamitsos, K. Clarke, S. Neubauer, H. Watkins, Exacerbation of cardiac energetic impairment during exercise in hypertrophic cardiomyopathy: a potential mechanism for diastolic dysfunction, Eur. Heart J. (2015), https://doi.org/10.1093/eurheartj/ehv120.